Applied Catalysis A, General 711 (2026) 120756

Contents lists available at ScienceDirect

Applied Catalysis A, General

journal homepage: www.elsevier.com/locate/apcata

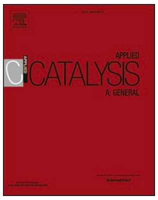

Catalyst development for the hydrogen to propylene oxide process with in-situ generated hydrogen peroxide and intensification in a trickle bed reactor

Christoph Schmidt [a], Francesco Sandri [a], Alice Vidrequin [b], Jeremy Favier [b], Atte Aho [a], Sari Granroth [c], Mika Lastusaari [d], Tapio Salmi [a,*]

[a] Laboratory of Industrial Chemistry and Reaction Engineering, Åbo Akademi University, Åbo, Turku 20500, Finland
[b] Faculté des Sciences Fondamentales et Appliquées, Université de Poitiers, Poitiers 86073, France
[c] Department of Physics and Astronomy, University of Turku, Åbo, Turku 20014, Finland
[d] Intelligent Materials Chemistry Group, University of Turku, Åbo, Turku 20014, Finland

ARTICLE INFO

Keywords:
One-pot synthesis
Propylene oxide
Hydrogen peroxide
Gold-palladium catalyst
Titanium silicalite
Trickle bed

ABSTRACT

Novel continuous propylene oxide production via in-situ generated hydrogen peroxide under mild liquid phase conditions was optimized by tailoring gold-palladium on titanium silicalite 1 (TS-1) catalysts and reaction parameters. AuPd alloy nanoparticles were deposited on two commercial TS-1 supports, with and without anatase impurities. On anatase-free TS-1, highly dispersed AuPd nanoparticles (6–10 nm) were formed, whereas in anatase-containing TS-1, metal precursors preferentially deposited on anatase, yielding larger nanoparticles after calcining. Ammonium hydroxide and water, water-only washing, and no washing were applied after synthesis, with water-only washing yielding smallest nanoparticles. Prolonged urea-deposition synthesis promoted metal redispersion, confirmed by material sampling during synthesis, and improved catalyst stability. In the combined direct synthesis of hydrogen peroxide and hydrogen peroxide to propylene oxide process (HPPO), smaller AuPd nanoparticles enhanced propylene oxide production but decreased propylene oxide selectivity by formation of propane and ring-opening products. Au-richer alloys improved propylene oxide selectivity but decreased propylene oxide productivity, while monometallic gold was inactive in the reaction system. Higher metal loadings increased propylene oxide productivity only for gold-richer alloys. Reaction parameter optimization identified that higher temperature and reduced liquid flow rate favored hydrogen peroxide conversion and ring-opening products formation, while shifting from propene-rich to oxygen-rich feed suppressed propane formation.

1. Introduction

Propylene oxide (PO) is a colorless, flammable, and highly reactive chemical [1]. Because of its reactivity, it is a key intermediate in several chemical processes, making it one of the most important building blocks in the chemical industry [2]. PO is mainly used for the production of polyether polyols, glycol and glycols ethers, which serve as precursors for polyurethane foams, antifreeze, coatings, lubricants, adhesives, inks and cosmetics [3,4]. Several industrial processes meet the demand for PO, including chlorohydrin as main contributor, styrene monomer, tert-butyl alcohol, and cumene-based process [5]. These processes can cause significant environmental issues due to the use of highly corrosive and toxic chorine as reactant or the involvement of highly toxic peroxo-species. The hydrogen peroxide to propylene oxide (HPPO) process, in which propene is oxidized with hydrogen peroxide in methanol over a titanium silicalite 1 (TS-1) catalyst, is considered as an environmental-friendly process and therefore the most growing PO production route [6].

The development of TS-1 by Taramasso et al. in 1983 was a breakthrough in material science and catalysis, as the material contains tetrahedrally coordinated Ti in a mordenite framework inverted (MFI) structure, which can activate hydrogen peroxide (H_2O_2) in contrast to numerous materials that only facilitate H_2O_2 decomposition. TS-1 opened a range of environmental-friendly oxidation processes with H_2O_2, for instance the HPPO process, with only water as by-product. The avoidance of toxic stoichiometric by-products makes the HPPO process

---

* Corresponding author.
E-mail address: tapio.salmi@abo.fi (T. Salmi).

https://doi.org/10.1016/j.apcata.2025.120756
Received 12 November 2025; Received in revised form 18 December 2025; Accepted 20 December 2025

an attractive PO production route, which offers a straightforward process design with low capital and operating costs [7]. Although the HPPO process is well established, catalyst development, process intensification and mechanistic investigation remain active research topics [8–12]. The drawback of the process is the use of expensive H_2O_2. To combat this issue in propylene oxide production, DOW-BASF has developed a process, in which the H_2O_2 production via anthraquinone process is integrated into the HPPO process [13], which improved the overall efficiency of the HPPO process.

The anthraquinone process is currently the only process which produces H_2O_2 on an industrial scale. However, side reactions of the organic catalyst and accumulation of impurities require a continuous exchange of the solvent, which lowers the process efficiency and causes serious environmental concerns. The direct synthesis of hydrogen peroxide (DSHP) with hydrogen and oxygen is a potential candidate to replace the anthraquinone process for on-site production of H_2O_2. The process is simple structured, similar to the HPPO process, with only reactants, inert gas, solvent, and catalyst, which enables coupling to existing processes. To obtain H_2O_2 from hydrogen and oxygen, selectivity enhancer, e.g. halide-ions or co-solvents, are needed to reduce the activity of Pd catalysts to suppress over-oxidation to water, as Pd also catalyzes direct oxidation of hydrogen to water, H_2O_2 hydrogenation and H_2O_2 decomposition. In the perspective to couple the DSHP to other processes, the use of bimetallic alloys as active phase is most suitable for enhancing the H_2O_2 selectivity. Several alloy compositions have been studied, which identified gold-palladium alloys as most productive [14], where the synergistic effect of gold significantly reduced the O-O cleavage, which causes water formation. While reducing the Pd content in the AuPd alloy improved the H_2O_2 selectivity; monometallic Au catalyst is almost inactive in H_2O_2 production, showing the need for Pd to activate hydrogen.

Nevertheless, the first report of propylene oxide production in the presence of hydrogen and oxygen in gas phase was published by Haruta's group, using Au/TiO_2 catalysts in a quartz tube reactor at 50 °C and atmospheric pressure [15]. However, this approach suffered from low propene conversion and low PO yield. Recent studies with improved conversions mostly perform the one-pot reaction at high temperature in gas phase or in supercritical CO_2[16–19], which require a high-energy input to reach the harsh reaction conditions. In our previous work, we introduced the novel one-pot process hydrogen to propylene oxide (HyPO) over in-situ generated H_2O_2, which combines DSHP and HPPO process. The HyPO process was conducted over a bifunctional AuPd/TS-1 catalyst in a trickle bed reactor under mild conditions of 8 bar and 10 °C and achieved PO productivity of $0.71\ \text{mol}\cdot\text{h}^{-1}\cdot\text{kg}_{\text{cat}}^{-1}$ with 43.4 % propene conversion and 26.5 % PO selectivity [20]. The combination of both active sites, AuPd for DSHP and tetrahedrally coordinated Ti for HPPO process, in a single catalyst could successfully run the consequential H_2O_2 generation and propene epoxidation as one-pot. However, the catalyst design needs improvement, as the main challenge of the HyPO system was undesired propene hydrogenation, which reduced PO selectivity.

In the current work, new AuPd/TS-1 catalysts were designed to improve the PO selectivity while maintaining a high catalyst activity. In addition, the process conditions, including temperature, liquid flow rate and reactant composition, were optimized, allowing a depth insight of the reaction dynamics of the consequential reaction steps in HyPO, illustrated in Fig. 1.

2. Materials and methods

2.1. Materials

AuPd/TS-1 catalysts were synthesized using two commercial titanium silicalite 1 (both TS-1, ACS Materials), in which lot 1 contained anatase impurities as a minor separate phase, while lot 2 was anatase-free. Further, hydrogen tetrachloroaurate(III) trihydrate (Thermo Fisher scientific, 99.99 %), palladium chloride (Alfa Aesar, 99.9 %), urea (Sigma-Alrich, 99.5 %), hydrochloric acid (Sigma-Alrich, ≥37 %), ammonium hydroxide (Emplura, 32 %) and deionized water was used for the catalyst synthesis. Silver nitrate (Sigma-Alrich, 99.0 %) was used for chloride ion detection. In catalytic experiments, quartz wool (Roth), glass wool (Merck), and quartz sand (Supelco) were used as packing materials in the reactor tube. The reactants, i.e. hydrogen (Woikoski, customized mixture of 4.89 % and 5.78 % hydrogen in CO_2), oxygen (Woikoski, 99.999 %) and propene (Linde, 99.5 %) were dissolved in methanol (Sigma-Alrich, ≥99.9 %) while carbon dioxide (Woikoski, 99.995 %) served as the inert gas. Argon (Woikoski, 99.999 %) was used for pressure regulation. Propylene oxide (Sigma-Aldrich, 99.9 %) and 1-methoxy-2-propanol (Sigma-Aldrich, >99.5 %) were used for calibration. Titanium(IV) oxysulfate (Sigma-Aldrich, 27 – 31 % sulfuric acid solution) was used for hydrogen peroxide analysis. The water content was analyzed by Karl-Fischer-titration using Hydranal™ Composite 2 and Hydranal™Methanol dry (Honeywell/Fluka).

2.2. Catalyst preparation

AuPd/TS-1 catalysts were synthesized by co-precipitation with urea to introduce the metal onto the support material. In a typical synthesis, $PdCl_2$ (3.33 mg) was dissolved with a few drops of concentrated HCl, followed by dilution with deionized water (200 ml). The solution was heated to 60 °C and sonicated before adding $HAuCl_4 \cdot 3\ H_2O$ (75.98 mg). The flask was covered with an aluminum foil which was kept throughout the synthesis. Subsequently, urea (5.05 g) and TS-1 (3.96 g) were added, and the pH was measured after each addition. The slurry was stirred vigorously at 250 rpm for 30 min before heating to 80 °C. After 4–18 h of heating, the slurry was cooled down for 1 h under continuous stirring, filtered and, depending on the catalyst, washed either with 32 % NH_4OH followed by deionized water, with water only, or not washed at all. Washing was continued until the chloride ion test was negative. The solid dried overnight at 60 °C in a rotary evaporator under vacuum. Finally, the dried solid was calcined at 300 °C for 3 h with a heating rate of 10 °C·min^{-1}. The prepared catalysts are listed in Table 1. The catalyst nomenclature indicates the nominal metal loading, nominal alloy composition, and TS-1 lot, while the suffixes N, W and nw refers to

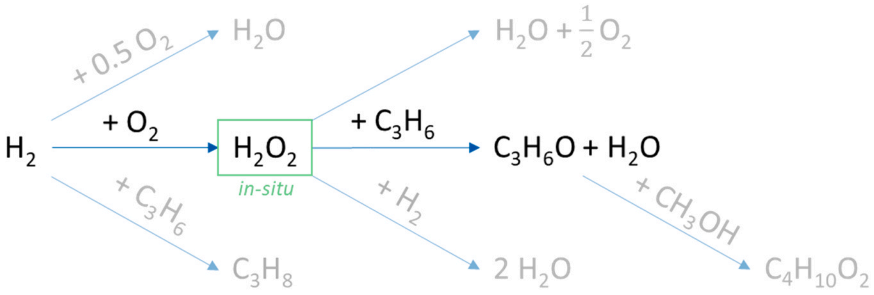

Fig. 1. Reaction scheme of combined DSHP and HPPO with side reactions.

Table 1
Synthesis procedures of gold-palladium (AuPd) catalysts from different titanium silicalite (TS-1) lots, synthesis time, washing procedure, nominal AuPd loadings and alloy composition. The investigated features are blue highlighted.

Catalyst name	TS-1	Synthesis time in h	Washing	Nom. AuPd loading in wt%	Nom. Au:Pd
$0.5Au_{90}Pd_{10}$-$TS1_{1}$-N[a]	Lot 1	15	NH_4OH + Water	0.5	90:10
$0.5Au_{90}Pd_{10}$-$TS1_{1}$-W[a]	Lot 1	15	Water	0.5	90:10
$0.5Au_{90}Pd_{10}$-$TS1_{1}$-4[b]	Lot 1	4	Water	0.5	90:10
$0.5Au_{90}Pd_{10}$-$TS1_{1}$-18[b]	Lot 1	18	Water	0.5	90:10
$0.5Au_{95}Pd_{05}$-$TS1_{1}$	Lot 1	15	Water	0.5	95:05
$0.5Au_{95}Pd_{05}$-$TS1_{2}$	Lot 2	18	Water	0.5	95:05
$1.0Au_{90}Pd_{10}$-$TS1_{2}$	Lot 2	13.5	Water	1.0	90:10
$1.0Au_{95}Pd_{05}$-$TS1_{2}$	Lot 2	13.5	Water	1.0	95:05
$1.0Au_{100}$-$TS1_{2}$	Lot 2	13.5	Water	1.0	100:0
$0.5Au_{90}Pd_{10}$-$TS1_{2}$-W[c]	Lot 2	13.5	Water	0.5	90:10
$0.5Au_{90}Pd_{10}$-$TS1_{2}$-nw[c]	Lot 2	13.5	no washing	0.5	90:10

[a, c] originated from one synthesis batch, with changed washing procedure after synthesis

[b] originated from one synthesis batch, part of the material was separated from the slurry to produce catalyst with lower synthesis time

washing with ammonium hydroxide and water, water only or no washing, respectively, and 4 and 18 denote the synthesis time in hours.

2.3. Catalyst characterization methods and procedures

Powder X-ray diffraction patterns (PXRD) were collected using PANalytical Aeris powder X-ray diffractometer equipped with PIXcel1D-Medipix3 detector by using Cu-K$_{\alpha1,\alpha2}$ radiation (λ = 1.5406 Å, 1.5444 Å). A 1/4° fixed divergence slit was used. Samples were prepared on a Si zero-background sample holder, and experimental data were recorded in the 2θ-range of 3–60° using a step size of 0.02° and counting time of 58.4 s per step. PXRD patterns were analyzed using the High-Score software suite [21] and the reference patterns were acquired from the international centre for diffraction data (ICDD) PDF-4 + database [22]. The morphology studies were conducted with scanning electron microscopy (SEM) with energy dispersive X-ray spectroscopy (SEM-EDS) (Zeiss Leo Gemini 1530) and transmission electron microscopy (TEM) (JEOL JEM-1400Plus). For the TEM examination, the samples were dispersed in ethanol and sonicated before being deposited onto the grids. The obtained images were processed and analysed by the software ImageJ to determine the AuPd nanoparticle sizes. The elemental analysis of the bulk material was performed with inductively coupled plasma - optical emission spectrometry (ICP-OES) (Agilent 5110 ICP-OES) and ion chromatography (IC). For ICP, the absorbances of silicon, aluminum and titanium were measured with radiation sources at wavelengths 288.2, 396.2, and 334.9 nm, respectively. Elemental compositions were calculated using the calibration curves generated from known standard solutions. IC was calibrated with two standard chloride solutions.

The oxidation states of gold, palladium, and titanium were determined by X-ray photoelectron spectroscopy using a NEXSA XPS (Thermo Fischer Scientific) for the fresh and spent catalysts. Al K$_\alpha$ radiation was used for the measurements with a spot size of 400 μm. Peak fitting was done with XPSPeak4.1 software. Prior to peak fitting, the Shirley background was subtracted from the data. Adventitious carbon C 1 s peak at 284.8 eV was used as a reference peak to take possible sample charging into account. The coordination of the titanium species of the TS-1 based materials was conducted via UV–vis diffuse reflectance spectroscopy (UV–vis DRS). For the measurements, the reflectance spectra were measured with an Avantes Avaspec HS-TEC CCD spectrometer through an Avantes FC-UV600–1-SR fiber optic cable. The light source was an Avantes AvaLight-DHc employing deuterium and halogen lamps. An Edinburgh Instruments $BaSO_4$ disc was used as the white reference. The absorbance was calculated from the reflection spectra according to the Kubelka-Munk theory. The signal was processed with the Savitzky-Golay smoothing algorithm with a window size of 10 and normalized to [0,1]. The surface area and porosity were determined by nitrogen physisorption (Micrometrics 3Flex-3500) using the Dubinin-Radushkevich method for calculating the specific surface area and density functional theory (DFT) to determine the pore volume and pore size distribution, assuming a cylindrical pore shape. Before the measurements, the samples underwent *ex-situ* degassing, being treated at 0.1 mbar and 180 °C for 24 h.

2.4. Setup of catalytic experiments

Catalytic experiments were performed in a setup with an integrated co-current trickle bed reactor (TBR), 30 cm long with 12 mm internal diameter and made of AISI 316 stainless steel, as illustrated in Fig. 2. Temperature control between −20 °C and 100 °C was allowed by a copper coil surrounding the reactor and connected to an external thermostat (Grant LT D6G). The gas flow rates were regulated with calibrated mass flow controllers (MFC) (Brooks 5866 and 5850 series), while methanol, being the liquid phase, was fed with a high-pressure liquid metering pump (Eldex ReciPro Series 2000). The reactor was equipped with a thermocouple for temperature monitoring, and the reactor pressure was regulated by a backpressure controller (BPC) (U3L Ultra Low Flow Back Pressure Regulator) installed downstream of the reactor. A sample line and a “night line” were implemented after the BPC. In the sample line, the gas and liquid phases were separated in a

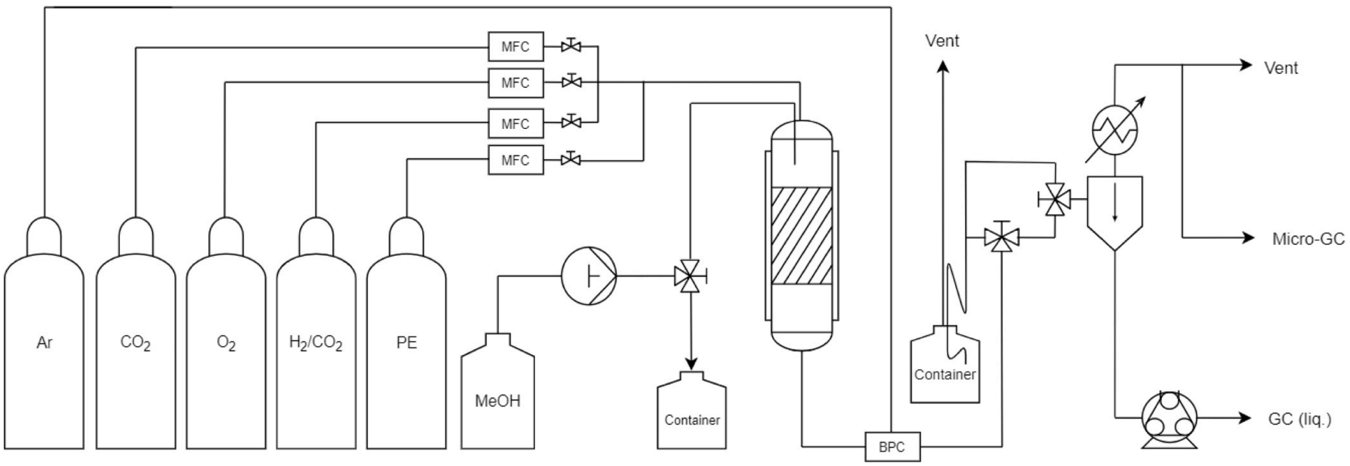

Fig. 2. Experimental setup for HyPO with mass flow controller (MFC), backpressure controller (BPC), gas chromatograph (GC), propene (PE), and methanol (MeOH).

three neck-round flask equipped with a condenser to recover volatile compounds and prevent the micro gas chromatograph (micro-GC) from exposure to liquids. The coolant temperature was set to −5 °C. The liquid phase was withdrawn from the gas-liquid separator with a pump (Heidolph Pumpdrive 5206) for sampling. In the “night line”, the gas and liquid phases were continuously separated by a double siphon, with the liquid collected in a bottle, while the gas stream flowed continuously, enabling online-analysis with the micro-GC.

2.5. *Chemical analysis*

The gas analysis was performed using a micro gas chromatograph (MicroGC, Agilent 490) with a thermal conductivity detector (TCD) and four capillary columns (10 m MS 5 A, 6 m 5CB, 10 m Al_2O_3/KCl, and 10 m PPU). The columns were operated at 80 °C with helium as the carrier gas, except for the molecular sieve column operated at 100 °C with nitrogen as the carrier gas. Hydrogen, oxygen, propene, and CO_2 were quantified by one-point calibration using ten replicate samples each. The response factor of propane was assumed to be equal to that of propene because their thermal conductivities differ by only 0.0015 $Wm^{-1}K^{-1}$[23].

The liquid phase analysis was carried out with a gas chromatograph (GC, Agilent 6890 N G1540N) equipped with a Plot U column (60 m length, 530 μm diameter, and 20 μm active phase thickness), operated at 185 °C. The propylene oxide and 1-methoxy-2-propanol calibration were conducted with the concentrations of 0.01–1 wt% in methanol, each measured twice. The amount of H_2O_2 was quantified by mixing a weighted sample with 0.5 ml of titanium oxysulfate solution. The formed yellow complex was diluted to 10 ml with water and the absorbance at 409 nm was measured with a UV–vis spectrometer (Shimadzu UV-2600i). A reference solution with 2 ml methanol, 0.5 ml titanium oxysulfate diluted to 10 ml was used in the double beam setup. The calibration was performed according to the reference procedure [24]. The water analysis was conducted by Karl-Fischer titration. The titrator (Metrohm 736 GP Titrino) was calibrated before the experiment with three injections of 10 μl water. The methanol, used as the reaction solvent, was analysed with three injections of 0.5 ml to distinguish reaction-formed water from the water content in methanol.

2.6. *Catalytic experiments*

Hydrogen and oxygen can form explosive gas mixtures. For this reason, CO_2 was used as inert gas, which significantly reduces the flammability and enhances the solubility of the other gases present in the system [25]. For safety, hydrogen was supplied premixed with CO_2 to ensure constant dilution with oxygen. Prior to the experiments, the reactor walls were passivated by four successive fillings with 30 % HNO_3 to mask active iron species, preventing H_2O_2 decomposition [26]. All catalytic experiments were carried out in the tubular reactor described in Section 2.4. The reactor was packed from bottom to top with: glass wool, quartz sand (125 – 250 μm), quartz wool, the catalyst layer, quartz wool, and quartz sand (125 – 250 μm). The catalysts were pelletized and sieved to 32 – 63 μm. The catalyst layer was prepared by diluting 1 g of catalyst with 20 g of quartz sand (< 125 μm) to enhance heat transfer and hydrogen efficiency [27]. The lower sand layer held the catalyst bed in the reactor center, while the upper facilitates the mass transfer of the gases into the liquid.

A typical experiment was started by pressurizing the reactor with CO_2 and setting the cryostat to 10 °C. Once the pressure and temperature had been stabilized, the methanol flow was switched on. After reaching 8 bar and observing the first methanol droplet at the outlet, the catalyst bed was wetted for one hour. The reaction was initialized by switching to the reactant gas mixture, typically composed of 0.07 $mmol{\cdot}min^{-1}$ H_2, 0.07 $mmol{\cdot}min^{-1}$ O_2, 0.14 $mmol{\cdot}min^{-1}$ propene and 1.46 $mmol{\cdot}min^{-1}$ CO_2 with a total volumetric flow rate of 40 $ml{\cdot}min^{-1}$ at atmospheric pressure. For certain experiments the propene flow rate was 19 % reduced (0.114 $mmol{\cdot}min^{-1}$) due to a technical issue of the mass flow controller. In the flow rate experiments, the methanol flow rate of 0.5, 1 and 2 $ml{\cdot}min^{-1}$ were used, maintaining the operation condition within the trickle flow regime [28]. The reaction temperature ranged from 0 to 20 °C. For the reactor shutdown, the reactant gas mixture was switched to CO_2, maintaining the pressure and cooling. After 30 min flushing with CO_2, the methanol flow rate and the reactor cooling were stopped. Then, the reactor was stepwise depressurized to atmospheric pressure after 1 h, and the CO_2 gas flow was stopped. The reaction progress was continuously monitored by online gas analysis and liquid sampling to capture both the transient and steady states behavior of the system.

The conversion of hydrogen, oxygen and propene were calculated from the equation

$$X[\%] = \frac{\dot{n}_{\mathrm{in}} - \dot{n}_{\mathrm{out}}}{\dot{n}_{\mathrm{in}}} \times 100 \tag{1}$$

where $\dot{n}_{\mathrm{in}}$ and $\dot{n}_{\mathrm{out}}$ are the molar flow rates at the reactor inlet and outlet, respectively.

The selectivity of propylene oxide (PO) was defined as

$$S\ [\%] = \frac{\dot{n}_{\mathrm{PO}}}{\dot{n}_{\mathrm{PO}} + \dot{n}_{\mathrm{PA}} + \dot{n}_{\mathrm{ROP}}} \times 100 \tag{2}$$

where $\dot{n}_{\mathrm{ROP}}$ denotes the molar flow rate of ring-opening products (ROP), including 2-methoxy-1-propanol and 1-methoxy-2-propanol and $\dot{n}_{\mathrm{PA}}$ the propane (PA) molar flow rate.

The production is defined as the molar flow rate of the individual products H_2O, H_2O_2, PO, PA, and ROP, giving by

$$\dot{n} \quad [mols^{-1}] = \quad c \bullet \dot{V} \tag{3}$$

where c is the concentration and $\dot{V}$ is the volumetric flow rate.

The productivity is defined as the production normalized on the amount of metal in the system and expressed as

$$P \quad [mols^{-1} \quad g^{-1}] = \quad \frac{\dot{n}}{m_{cat} \bullet x_{loading}} \tag{4}$$

where m_{cat} is the catalyst mass and $x_{loading}$ is the metal loading.

3. Results and discussion

3.1. Catalyst synthesis and characterization

The catalyst synthesis method was based on our previous work [20], in which the urea co-precipitation was successfully applied to obtain small bimetallic nanoparticles. In the present study, the procedure was simplified; the dissolution of $PdCl_2$ was enhanced by heating and sonication, and the adjustment of the metal precursor solution to pH 2 with ammonium hydroxide was omitted. In all the synthesis batches, no premature precipitation was observed at pH 2.6 – 3.0 after the addition of TS-1 and urea unlike in our previous work at pH 2.5. The method was proved suitable for different catalyst batch sizes (3–10 g), as all batches were successfully neutralized (pH 7.9 – 8.7) by urea hydrolysis, leading to metal deposition on the support materials. A detailed overview of the catalyst amounts and measured pH changes is reported in the supplementary material S 1.

The urea deposition method was selected because of the efficient chloride removal with ammonium-ions, originating from the urea decomposition, and the complete degradation of urea during calcination, in contrast to NaOH, avoiding any influence of ions that could act as selectivity enhancers and promoters on the reaction system. Further, the urea deposition method follows a re-deposition mechanism reported by Zanella et al. [29], resulting in highly dispersed Au nanoparticles. To investigate this mechanism in the present system, slurry samples were withdrawn after 1, 2, 4, 5 and 18 h of the synthesis batch, and the pH was measured. Each sample was subsequently washed with water, filtered, dried and calcined following the standard catalyst preparation procedure. The ICP and TEM results of the obtained catalysts are shown in Fig. 3. During the first hour, the pH increased slightly from 2.8 to 3.5 due to the heating period to 80 °C. At this initial stage, metal deposition had already begun, as confirmed by a metal loading of 0.17 wt%. After the first hour, the pH increased sharply, followed by a flattening increase to 8.5. Despite this increase, the metal loading decreased after 2 h. TEM analysis revealed a decrease of AuPd nanoparticle sizes on TS-1 between 1 and 5 h and on anatase after 2 h. The metal deposition on the two distinct phases, considering anatase as an impurity, will be discussed later in this section. The observed decrease in AuPd nanoparticle size is described as fragmentation process in which the initially large metal precipitates deaggregate as their surface charge and interaction with the support change with increasing pH [29]. The process is likely enhanced by complexation of the metal precipitates with urea deposition products, which might partially re-dissolve the deposited metal species, explaining the decreasing metal loading, and subsequently re-adsorb at higher pH. This mechanism promotes high dispersion, resulting in smaller nanoparticles after calcining. This is clearly reflected in the particle size distributions in Fig. 4, which became after 2 h narrower and shifted towards smaller sizes, decreasing the fraction of larger particles. After 18 h, the metal loading increased again, indicating that the re-deposition was complete. At this stage, sintering of the AuPd nanoparticles was observed on TS-1, while on anatase, the AuPd mean size remained unchanged, indicating a lower mobility of the nanoparticles on its surface due to a stronger metal-support interaction.

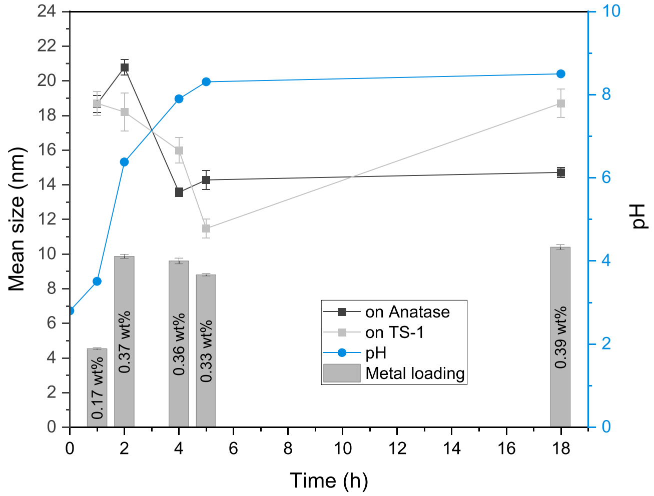

Fig. 3. The pH evolution during the catalyst synthesis of $0.5Au_{90}Pd_{10}$-$TS1_1$-1, −2, −4, −5 and −18 (blue, circle) at various times, with the corresponding metal loading (grey bars) and AuPd particle mean size on anatase (dark grey, square) and TS-1 particles (light grey, square).

The crystallinity of the synthesized catalysts and commercial TS-1 materials was investigated with powder X-ray diffraction (PXRD). All the samples showed the characteristic MFI diffraction patterns, with reflections at $2\Theta = 7.9^\circ$, 8.8°, 23.0°, 23.9° and 24.4° [30], as displayed in Fig. 5. Traces of anatase, determined to be 0.33 vol%, were detected at 25.3° in TS-1 lot 1 ($TS1_1$) and in the catalysts Au_xPd_y-$TS1_1$, while this reflection was absent in TS-1 lot 2 ($TS1_2$) and the catalysts Au_xPd_y-$TS1_2$.

The TS-1 morphology and distribution of AuPd nanoparticles was studied with SEM. Distinct differences in the shapes of TS-1 were observed in Fig. 6a-b. In $TS1_1$, the TS-1 crystals appeared as cauliflower-like spheres with diameters between 150 and 300 nm, whereas in $TS1_2$, they were shaped as stretched hexagonal prisms, ranging from 70 to 260 nm. Anatase appeared in $TS1_1$ as the minor phase in the form of cubes and ellipsoids (Fig. 6a, S 2). The AuPd alloy in the catalysts Au_xPd_y-$TS1_1$ show a high contrast against the support material, as clearly visible in the backscatter electron micrographs Fig. 6c-d. The bright AuPd nanoparticles are found around specific support particles, which show the predominant accumulation on anatase particles (Fig. 6c). The preferential deposition of metal on anatase sites, discussed in our previous publication [20], originated from the more positive zeta potential of anatase, which leads to a stronger attraction of metal precursors during synthesis. Interestingly, in $0.5Au_{90}Pd_{10}$-$TS1_1$-N, pre-washed with ammonium hydroxide, almost no isolated AuPd nanoparticles on TS-1 were observed unlike in $0.5Au_{90}Pd_{10}$-$TS1_1$-W, where AuPd nanoparticles were present on both TS-1 and anatase sites. The ammonium hydroxide pre-wash intended to anchor the precursors on the support prior to water washing [31]; however, the harsh chemical treatment possibly removed the weakly bound precursors from the TS-1 surface, indicating a weaker interaction with TS-1, consisted with the accumulation of AuPd nanoparticles on the anatase sites after calcining. In contrast, in the anatase-free $0.5Au_{90}Pd_{10}$-$TS1_2$-W, no metal particles were observed in the backscatter electron images (Fig. 6e), indicating the presence of highly distributed and small AuPd nanoparticles, which cannot be resolved by SEM. $0.5Au_{90}Pd_{10}$-$TS1_2$-nw, which is not washed, exhibited very large AuPd particles up to 1 µm (Fig. 6f), unlike the washed catalyst $0.5Au_{90}Pd_{10}$-$TS1_2$-W.

The size and distribution of supported AuPd nanoparticles were examined with TEM. Since the support materials differed, two separate nanoparticle size distributions were determined for the AuPd nanoparticles on anatase and on TS-1. As shown in Fig. 7, AuPd nanoparticles on TS-1 ranged from 4 to 16 nm, whereas those on anatase exhibited a much broader distribution from 1 to 48 nm, with mean sizes between 9

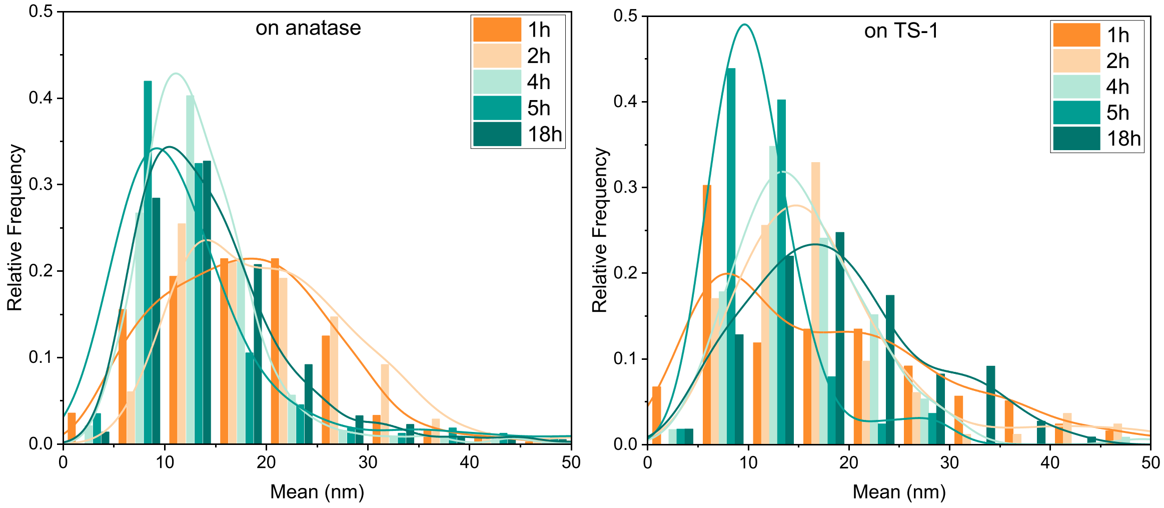

Fig. 4. AuPd nanoparticle size distribution with Kernel smoothing curves of $0.5Au_{90}Pd_{10}$-$TS1_1$-1, −2, −4, −5 and −18 synthesized at various times. The left graph shows the AuPd size distribution on anatase, and the right graph on TS-1.

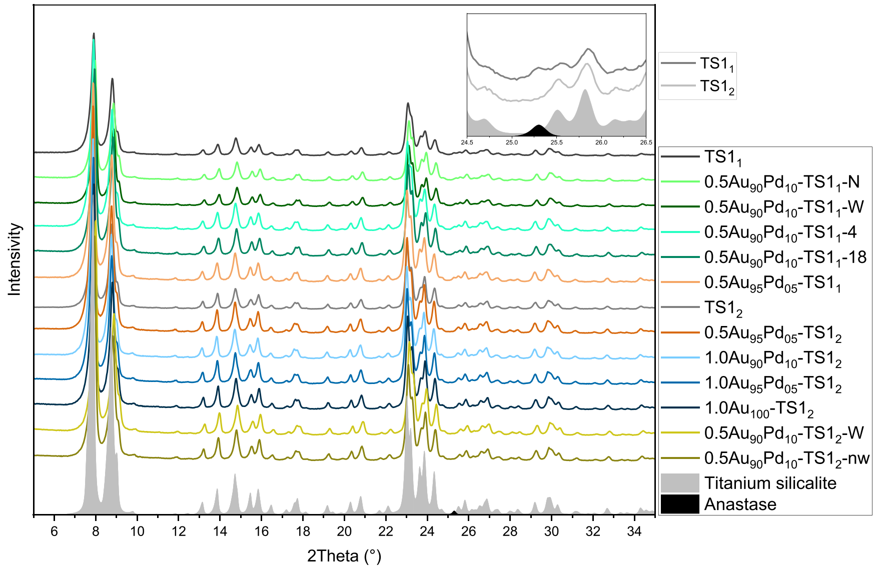

Fig. 5. XRD pattern of different TS-1 lots and AuPd/TS-1 catalysts. The simulated pattern of titanium silicalite (TS-1) (dark grey, Inorganic Crystal Structure Database (ICSD) 93539) and anatase (black, ICSD 121632) are shown on the bottom. Top-right are the magnified patterns of $TS1_1$ and $TS1_2$ with simulated patterns between 24.5 – 26.5°.

and 19 nm. The relatively large metal nanoparticles were formed because of concentrated deposition on anatase sites. In our previous study, we observed that a higher anatase amount significantly reduced the AuPd nanoparticle size, as the deposition was less concentrated on the anatase sites. The anatase-containing catalysts Au_xPd_y-$TS1_1$, showing in small amounts mostly isolated AuPd nanoparticles on TS-1 (Fig. 8a), while on anatase they appeared in a close proximity (Fig. 8b), which facilitated sintering and broadened their size distribution. In contrast, the catalysts Au_xPd_y-$TS1_2$ without anatase, exhibited well-dispersed AuPd nanoparticles across the TS-1 crystals (Fig. 8c).

Despite the higher AuPd nanoparticles density on the TS-1 sites, the AuPd mean sizes between 6.3 – 9.8 nm was smaller compared to the catalysts Au_xPd_y-$TS1_1$ with 9.1 – 18.7 nm (Table 2). The nanoparticle size found on TS-1 is large compared when other supports were used [29]. The repulsive interactions between the negatively charged TS-1 and the negatively charged metal precursor hinder a stable adsorption and promote mobility [20], which tends to form agglomerates. The growth is additionally promoted by calcination [32]. The different morphology of the TS-1 crystals in $TS1_1$ and $TS1_2$ (Fig. 6a-b), likely affected the nucleation and stability of AuPd nanoparticles. A similar morphology-depending particle size distribution for Au nanoparticles on TiO_2 was reported by Verma et al. [33]. $0.5Au_{90}Pd_{10}$-$TS1_2$-nw, synthesized without washing, contained AuPd either as very large particles or as small non-spherical nanoparticles with high transmission. The high transmission and irregular shape, observed in Fig. 8d, suggests that these nanoparticles were not fully reduced to the metal form [34], likely due to residuals of chloride ions. In contrast, the washed $0.5Au_{90}Pd_{10}$-$TS1_2$-W catalyst exhibited similarly sized but spherical nanoparticles and with low transmission, displayed in Fig. 8c, indicating a complete reduction to metallic AuPd.

The metal loading of the catalysts, determined by ICP analysis, ranged from 0.33 to 0.41 wt% for catalysts with a nominal loading of 0.5 wt% ($0.5Au_xPd_y$-$TS1_z$), except for $0.5Au_{90}Pd_{10}$-$TS1_1$-1, which showed a lower loading of 0.17 wt% after 1 h of synthesis (Table 2). For catalysts with a nominal loading of 1.0 wt% ($1.0Au_xPd_y$-$TS1_2$), the metal contents were determined between 0.60 and 1.0 wt%. The observation

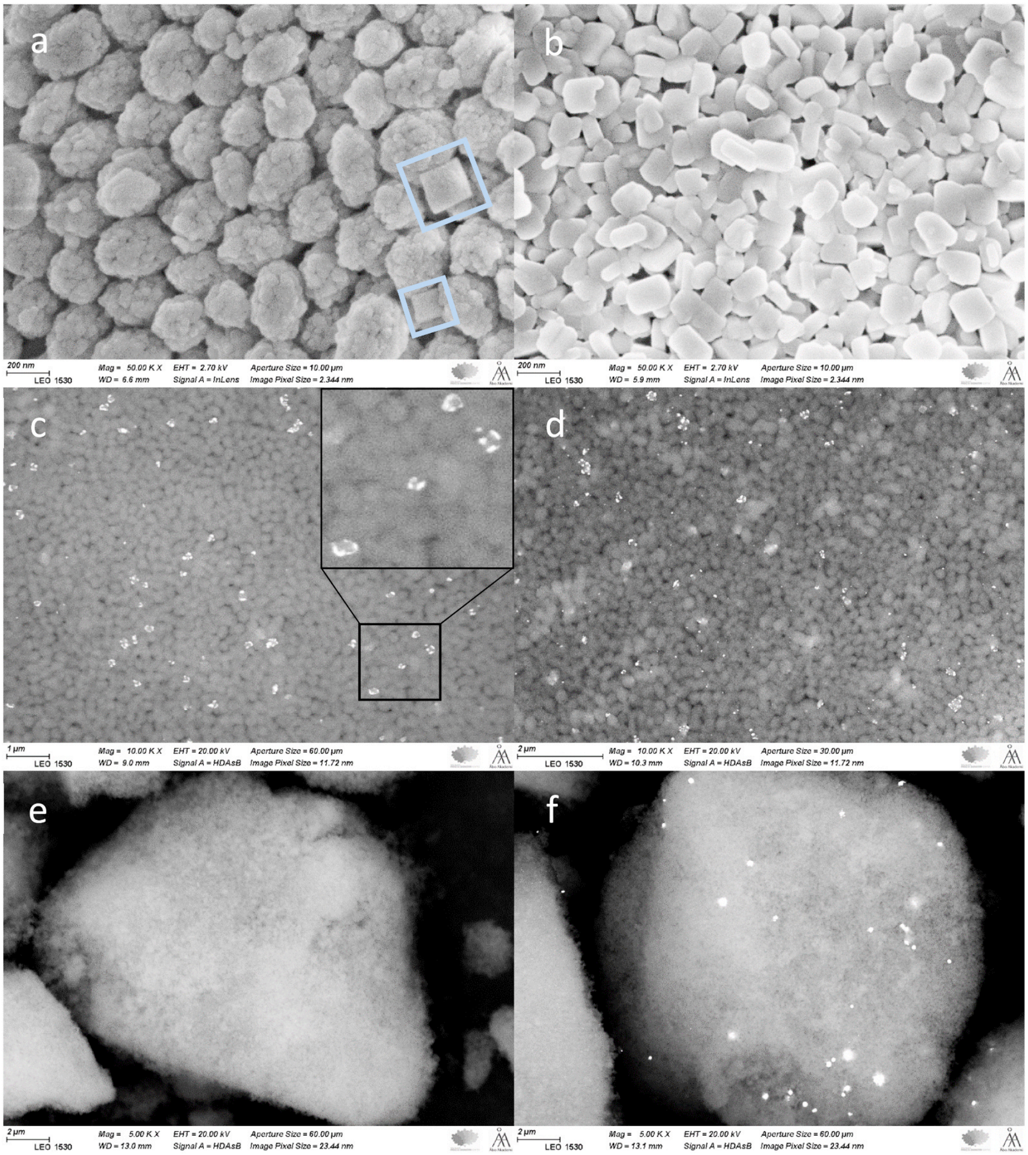

Fig. 6. Secondary electron micrographs of $0.5Au_{90}Pd_{10}$-$TS1_1$-18 with anatase as minor phase (blue frames) (a), $1.0Au_{95}Pd_{05}$-$TS1_2$ (b), and backscatter electron micrographs of $0.5Au_{90}Pd_{10}$-$TS1_1$-N (c), $0.5Au_{90}Pd_{10}$-$TS1_1$-W (d), $0.5Au_{90}Pd_{10}$-$TS1_2$-W (e), $0.5Au_{90}Pd_{10}$-$TS1_2$-nw (f).

that complete deposition is achieved with monometallic gold, while the degree of deposition decreases with increasing Pd content, suggests that Pd interferes with the metal deposition on TS-1 by promoting co-precipitation with Au in solution. Additionally, electrostatic repulsion between the negative charged metal complexes and negatively charged TS-1 surface likely contribute to the incomplete deposition. The Pd content of the AuPd alloys were close to the target compositions, except for $1.0Au_{90}Pd_{10}$-$TS1_2$, and the unchanged alloy composition at different synthesis times confirmed the uniform deposition of both metals. The different washing procedures had no effect on either the metal loading or the alloy composition, as shown by a comparison of catalysts from the same synthesis batch, $0.5Au_{90}Pd_{10}$-$TS1_1$-N and -W, as well as $0.5Au_{90}Pd_{10}$-$TS1_2$-W and -nw. The chloride content of the catalysts $0.5Au_{90}Pd_{10}$-$TS1_1$-N and –W was analyzed using ion chromatography and determined to be 39 and 74 ppm, respectively, indicating slightly more effective chloride removal when a prior ammonium hydroxide washing step was applied.

The oxidation states of the metals and the metal-support interaction were studied with XPS. For $0.5Au_{90}Pd_{10}$-$TS1_1$-W, the binding energies (BE) of Au 4 $f_{7/2}$ and Pd $3d_{5/2}$ were 83.8 eV and 334.9 eV, respectively, as shown in Fig. 9. These values correspond to the metallic states, indicating the alloy formation of Au and Pd, since Pd would be expected in the oxide form after calcination in air [35]. In the spectra, the Pd $3d_{5/2}$ and Au $4d_{5/2}$ peaks overlap [36]. A comparison of $0.5Au_{90}Pd_{10}$-$TS1_1$-4 and $0.5Au_{90}Pd_{10}$-$TS1_1$-18 reveals identical BE for Au and Pd, suggesting that the synthesis time did not affect the electronic state of the alloy. In contrast, the comparison of $0.5Au_{95}Pd_{05}$-$TS1_1$ and $0.5Au_{95}Pd_{05}$-$TS1_2$, prepared with nearly same synthesis times but different TS-1 lots, shows a 0.2 eV shift to higher BE for both the Au 4 $f_{7/2}$ and Pd $3d_{5/2}$ peak in $0.5Au_{95}Pd_{05}$-$TS1_1$. The lower BE of Au in $0.5Au_{95}Pd_{05}$-$TS1_2$, $0.5Au_{90}Pd_{10}$-$TS1_1$-18, −4, and -W indicate a stronger metal-support interaction, which can be explained by a charge transfer from the support to the alloy, increasing the electron density [37]. Interestingly, $0.5Au_{90}Pd_{10}$-$TS1_1$-18 and $0.5Au_{95}Pd_{05}$-$TS1_1$, both prepared with the same TS-1 lot, exhibited different Au BE, due to the gold-richer alloy of $0.5Au_{95}Pd_{05}$-$TS1_1$, shifting the BE to the standard value of 84 eV for metallic gold. The BE of Ti 2p $_{3/2}$ were found at 459.3 and 460.3 eV for $0.5Au_{90}Pd_{10}$-$TS1_1$-W, −4, −18 and $0.5Au_{95}Pd_{05}$-$TS1_1$, and at 458.8 and 460.1 eV for $0.5Au_{95}Pd_{05}$-$TS1_2$. The different coordination environments of the Ti species result in distinct BE, where 460.1 and 460.3 eV

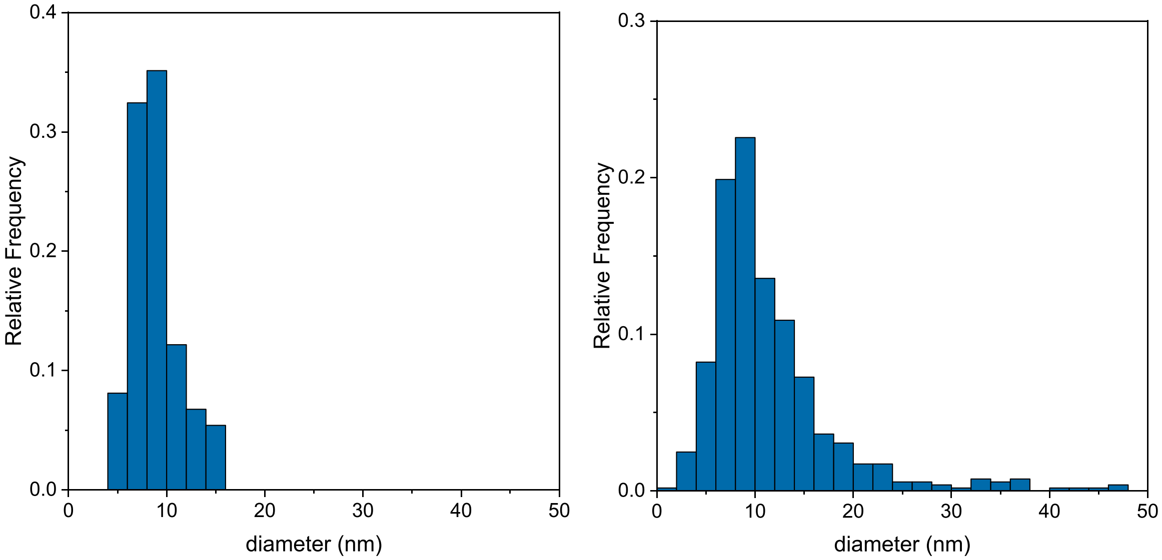

Fig. 7. AuPd nanoparticle size distribution on TS-1 (left) and on anatase (right) of $0.5Au_{90}Pd_{10}$-$TS1_1$-W.

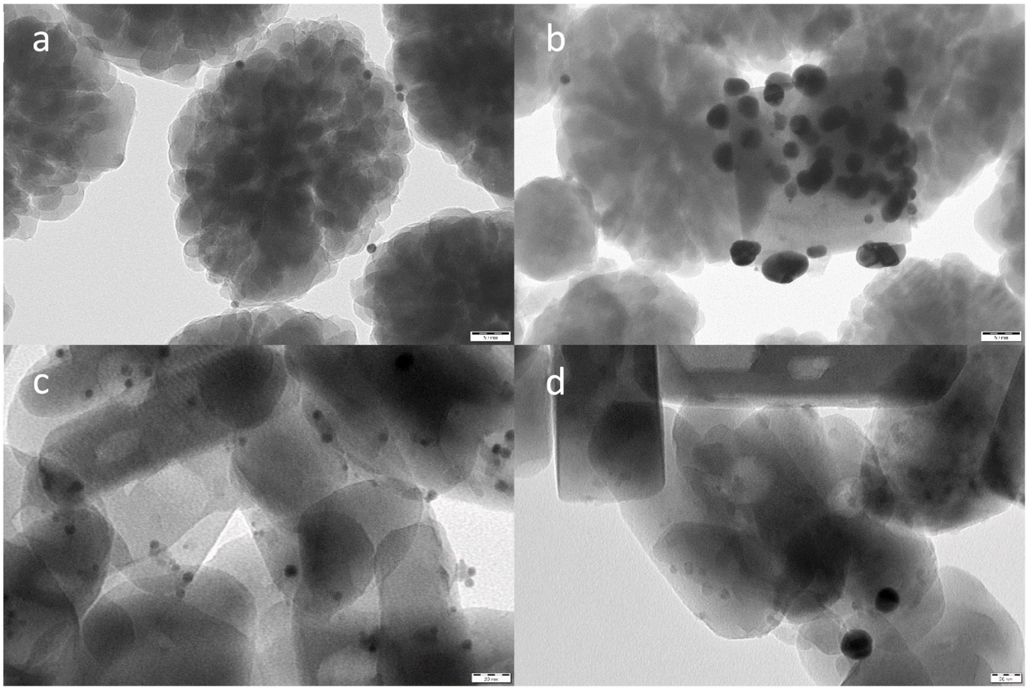

Fig. 8. Transmission electron micrographs of $0.5Au_{90}Pd_{10}$-$TS1_1$-4 (a, b), $0.5Au_{90}Pd_{10}$-$TS1_2$-W (c) and $0.5Au_{90}Pd_{10}$-$TS1_2$-nw (d).

can be assigned to tetrahedrally coordinated Ti, while 458.8 and 459.3 eV can be assigned to octahedral Ti-species [38]. The increased intensity of the peak at lower BE for $0.5Au_{95}Pd_{05}$-$TS1_2$, 458.8 – 459.3 eV, indicates the presence of a higher amount of octahedral coordinated Ti compared to $0.5Au_xPd_y$-$TS1_1$ catalysts.

The coordination of Ti species was analyzed by DRS UV–vis spectroscopy. The bands observed in $TS1_1$ and $TS1_2$ at 207 nm, 230 – 232 nm and 268–296 nm correspond to closed tetrahedral $Ti(OSi)_4$, open tetrahedral $Ti(OSi)_4OH$ and octahedral "TiO_6", $Ti(OSi)_4(OTiO_5)_2$, Ti species, respectively [39]. TiO_2 in the form of anatase was detected only in $TS1_1$ and Au_xPd_y-$TS1_1$ catalysts at around 335 nm, aligning with the XRD analysis. As shown in the magnified panels of Fig. 10, $TS1_1$ exhibited a slightly higher ratio of tetrahedrally to octahedrally coordinated Ti compared to $TS1_2$, consistent with the XPS results. The Ti_{tetra}/Ti_{octa} ratio is further increased in Au_xPd_y-$TS1_1$ catalysts, as the TiO_6 band region was attenuated. The decrease of the TiO_6 band, which indicates a re-coordination of Ti from octahedral to tetrahedral geometry, likely originated from the initial acidic conditions during the catalyst synthesis, which altered partially the Ti environment, favoring the hydrolysis of TiO_6 [39]. Interestingly, the spectra of the metal-modified Au_xPd_y-$TS1_2$ closely resembled those of $TS1_2$, suggesting that this material was not affected by the synthesis. In addition to the Ti-related bands, the surface plasmon resonance (SPR) band of AuPd was observed in $0.5Au_{95}Pd_{05}$-$TS1_1$ and all the catalysts prepared with $TS1_2$. The SPR intensity increased with higher Au content in the alloy, as Pd dampens the SPR, and was most pronounced in $1.0Au_{100}$-$TS1_2$, where only gold was deposited [40].

The surface properties of the materials were analyzed by nitrogen physisorption. The measured specific surface areas (SSA) were 514 m^2/g for $TS1_1$ and 441 m^2/g for $TS1_2$, while for metal-modified TS-1 materials

Table 2
The AuPd nanoparticle mean sizes on anatase and TS-1, metal loadings, and Pd contents in the alloys of different catalysts. The ratio of Au and Pd, and the nominal Pd contents are given in brackets.

Catalyst	AuPd nanoparticle size on anatase	AuPd nanoparticle size on TS-1	Metal loading (Au/Pd)[a]	Pd in alloy (nom.)[b]
	[nm]	[nm]	[wt%]	[%]
$0.5Au_{90}Pd_{10}$-$TS1_1$-N	15.1 ± 1.1	10.5 ± 0.9	0.37 (0.33/0.05)	12 (10)
$0.5Au_{90}Pd_{10}$-$TS1_1$-W	11.8 ± 0.3	9.06 ± 0.29	0.37 (0.33/0.05)	12 (10)
$0.5Au_{90}Pd_{10}$-$TS1_1$-1	18.7 ± 0.5	18.7 ± 0.7	0.17 (0.15/0.02)	11 (10)
$0.5Au_{90}Pd_{10}$-$TS1_1$-2	20.8 ± 0.4	18.2 ± 1.1	0.37 (0.33/0.04)	11 (10)
$0.5Au_{90}Pd_{10}$-$TS1_1$-4	13.57 ± 0.24	16.0 ± 0.7	0.36 (0.32/0.04)	11 (10)
$0.5Au_{90}Pd_{10}$-$TS1_1$-5	14.3 ± 0.5	11.5 ± 0.5	0.33 (0.30/0.04)	11 (10)
$0.5Au_{90}Pd_{10}$-$TS1_1$-18	14.71 ± 0.28	18.7 ± 0.8	0.39 (0.35/0.04)	11 (10)
$0.5Au_{95}Pd_{05}$-$TS1_1$	13.01 ± 0.27	15.6 ± 0.8	0.35 (0.33/0.02)	5 (5)
$0.5Au_{95}Pd_{05}$-$TS1_2$	-	6.26 ± 0.11	0.41 (0.39/0.02)	5 (5)
$1.0Au_{90}Pd_{10}$-$TS1_2$	-	7.04 ± 0.13	0.60 (0.51/0.09)	15 (10)
$1.0Au_{95}Pd_{05}$-$TS1_2$	-	9.42 ± 0.19	0.89 (0.85/0.05)	5 (5)
$1.0Au_{100}$-$TS1_2$	-	9.83 ± 0.16	1.00 (1.00/ -)	0 (0)
$0.5Au_{90}Pd_{10}$-$TS1_2$-W	-	5.56 ± 0.10	0.35 (0.31/0.04)	10 (10)
$0.5Au_{90}Pd_{10}$-$TS1_2$-nw	-	6.56 ± 0.19	0.34 (0.30/0.03)	10 (10)

[a] separate Au and Pd loading [wt%] in brackets
[b] nominal Pd content [%] in the alloy

the SSA ranged from 405 to 441 m^2/g, as reported in Table 3. Catalysts based on $TS1_2$ showed nearly unchanged values for the SSA after metal modification, whereas those based on $TS1_1$ exhibited a decrease of 73–109 m^2/g compared to the parent material. In Fig. 11, the isotherms of the Au_xPd_y-$TS1_1$ catalysts exhibit reduced hysteresis loops, indicating a decrease in mesoporosity consistent with the observed decrease of the SSA. The decreased pore volume is likely due to AuPd nanoparticles clogging the intraparticle channels of the cauliflower-like $TS1_1$ spheres, as shown in S 3. All the materials exhibited high porosities between 0.254 and 0.305 cm^3/g, with the micropores of the MFI structure contributing 74 – 86 % of the total porosity. $TS1_2$ and the catalysts Au_xPd_y-$TS1_2$ exhibited slightly lower pore volumes compared to the Au_xPd_y-$TS1_1$ catalysts and $TS1_1$, consistent with their lower SSA. This result is also reflected in the isotherm region at 0 – 0.1 p/p^0, where micropore condensation occurs; $TS1_1$ materials display a concave slope, whereas $TS1_2$ materials exhibit a convex one. The average pore width of 0.61–0.62 nm remained unchanged after the metal modification, confirming that the topology of the TS-1 materials was preserved, consistent with the XRD results.

3.2. Catalytic experiments in trickle bed reactor

In our previous work, important insights were already gained into the behavior of AuPd/TS-1 catalysts in the reaction system of HyPO [20]. It was found that H_2O_2 and propene hydrogenation play a major role even when using an $Au_{94}Pd_{06}$ alloy catalyst with a low Pd content, while the H_2O_2 decomposition was negligible. It was also found that an increased metal nanoparticle size decreased the activity in DSHP but enhanced the efficiency of HyPO by decreasing the undesired propene hydrogenation more than H_2O_2 production. Another important finding was that propene adsorbs on the metal sites, which are the active sites of DSHP, and competes with the H_2 and O_2 coverages, which significantly reduced H_2O_2 production in comparison with only H_2 and O_2 in the system. As the catalytic system substantially changed in the presence of propene, the H_2O_2 formation rates in the absence of propene were not determined in the present work to maintain the focus on the main object, the HyPO process. To elucidate the influence of the active site on HyPO, catalysts were prepared using different synthesis methods, resulting in different properties of the active sites, and compared in this work to derive structure-related activity of the catalyst.

3.2.1. Impact of catalyst synthesis

In the first investigation, an additional washing step with ammonium hydroxide was introduced in the synthesis of $0.5Au_{90}Pd_{10}$-$TS1_1$-N before washing with water, whereas $0.5Au_{90}Pd_{10}$-$TS1_1$-W was washed with water only. The catalytic performance of $0.5Au_{90}Pd_{10}$-$TS1_1$-N and $0.5Au_{90}Pd_{10}$-$TS1_1$-W, differed significantly, with the PO production of 3.4 and 6.2 µmol·min^{-1}, respectively, at 225 min time-on-stream (TOS) (Fig. 12).

The SEM analysis of $0.5Au_{90}Pd_{10}$-$TS1_1$-W revealed a higher density of AuPd nanoparticles on TS-1 compared to $0.5Au_{90}Pd_{10}$-$TS1_1$-N (Fig. 6c-d), which likely accounts for the increased O_2 conversion due to a larger active surface available for DSHP (Fig. 13, values in S 4). Despite the presence of fewer AuPd nanoparticles on TS-1 and larger nanoparticle mean sizes in $0.5Au_{90}Pd_{10}$-$TS1_1$-N compared to $0.5Au_{90}Pd_{10}$-$TS1_1$-W, a higher H_2 conversion and a shift in the product distribution were observed, with increased propane and reduced H_2O_2 formation (Fig. 14). This behavior can be related to the slightly lower content of 39 ppm residual chloride in $0.5Au_{90}Pd_{10}$-$TS1_1$-N compared to 74 ppm in $0.5Au_{90}Pd_{10}$-$TS1_1$-W, indicating more effective chloride removal by NH_4OH washing. Residual chloride acts as an inhibitor in the hydrogenation of propene by decreasing the Pd activity [41]; however, in DSHP, chloride and other halide ions are known to enhance the H_2O_2 selectivity [42]. The decreased selectivity is also observed in the H_2O_2 formation over time (S 5), in which after a spike in the beginning of the reaction, almost no H_2O_2 is detected in contrast to $0.5Au_{90}Pd_{10}$-$TS1_1$-W, showing a stable H_2O_2 production about 0.05 µmol/min. For the following experiments, the catalyst amount was doubled to better distinguish the differences in performance, and the reaction time was extended overnight, since PO production with $0.5Au_{90}Pd_{10}$-$TS1_1$-N had not yet stabilized after 230 min and to capture long-term effects in HyPO.

The effect of the synthesis time on the catalyst stability was investigated with $0.5Au_{90}Pd_{10}$-$TS1_1$-4 and $0.5Au_{90}Pd_{10}$-$TS1_1$-18. At 70 min TOS, $0.5Au_{90}Pd_{10}$-$TS1_1$-18 showed a slightly higher PO production compared to $0.5Au_{90}Pd_{10}$-$TS1_1$-4 (Fig. 12), likely due to the slightly higher metal loading of 0.03 wt%. While $0.5Au_{90}Pd_{10}$-$TS1_1$-18 maintained a stable PO production exceeding 11 µmol·min^{-1}, $0.5Au_{90}Pd_{10}$-$TS1_1$-4 deactivated gradually, as reflected by strongly reduced H_2 and O_2 conversions after 1420 min TOS (Fig. 13). The H_2O_2 production of $0.5Au_{90}Pd_{10}$-$TS1_1$-4 exhibited a typical spike in the beginning of the reaction (S 5), which was already observed in our previous study [20]· H_2O_2 cannot be converted until TS-1 is activated with H_2O_2, in which the tetrahedral Ti species is re-coordinated, becoming accessible for the epoxidation mechanism [43]. After the initial spike, $0.5Au_{90}Pd_{10}$-$TS1_1$-4 produced a constant amount of H_2O_2, while $0.5Au_{90}Pd_{10}$-$TS1_1$-18 showed a steady increase in H_2O_2 production. The activation in

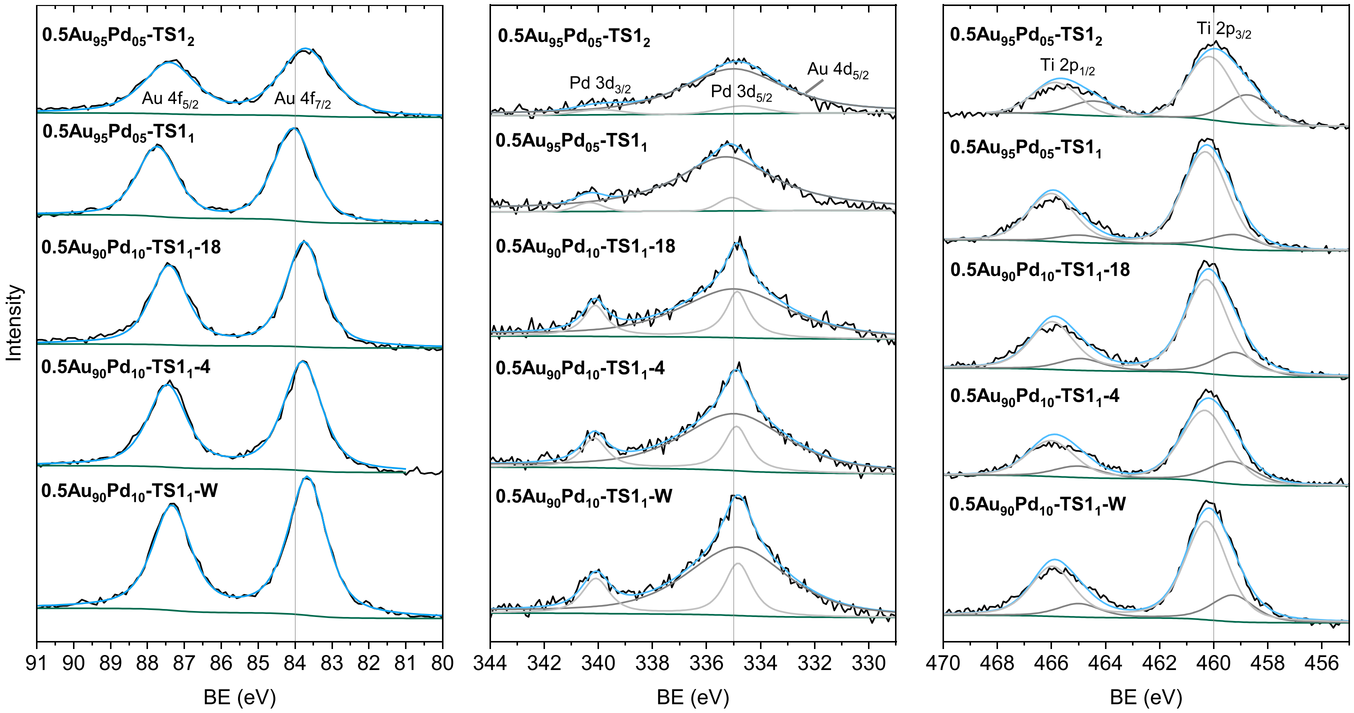

Fig. 9. XPS spectra of Au, Pd and Ti of different catalysts.

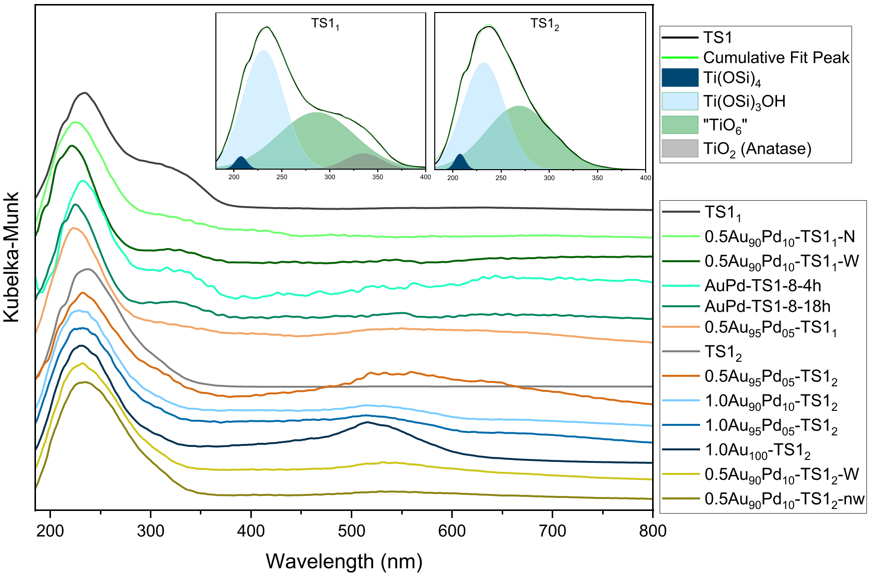

Fig. 10. DRS-UV–vis spectra of different catalysts and TS-1 materials. The magnified UV–vis spectra of TS1_1 (upper left panel) and TS1_2 (upper right panel), were deconvoluted with the different Ti species.

0.5$Au_{90}Pd_{10}$-TS1_1-18 is counteracted by a simultaneous deactivation in epoxidation, resulting in an overall stable PO production. In contrast, the stable H_2O_2 generation with 0.5$Au_{90}Pd_{10}$-TS1_1-4 result combined with the deactivation led to a gradual declining PO production, which aligns with the findings in our previous work. The deactivation and activation are discussed in detail in Section 3.2.6 Catalyst deactivation.

Using 0.5$Au_{90}Pd_{10}$-TS1_2-nw, prepared without washing, what is a typical procedure in DSHP studies [44,45], in HyPO resulted in a low PO production of 0.7 μmol·min^{-1} compared to 8.9 μmol·min^{-1} achieved with the washed catalyst 0.5$Au_{90}Pd_{10}$-TS1_2-W. The low PO production was reflected in a low H_2 conversion of 32.1 %, and 3.7 % O_2 conversion, whereas 0.5$Au_{90}Pd_{10}$-TS1_2-W completely converted H_2 and 30.4 % of O_2 at 1420 min TOS. SEM analysis (Fig. 6f) revealed large metal particles in 0.5$Au_{90}Pd_{10}$-TS1_2-nw, explaining the low catalytic activity due to the low surface-to-volume ratio and consequently reduced active surface for DSHP.

The comparison of different synthesis methods identified a post synthesis treatment with water only as the most effective approch to obtain highly active and selective catalysts for HyPO, as it yielded the highest nanoparticle dispersion and retained traces of chloride ions, which likely improved the H_2O_2 selectivity by suppressing water formation. In contrast, omission of any post synthesis washing resulted in the formation of large AuPd particles after calcination with a strongly decreased catalytic activity. With a longer synthesis time, catalyst

Table 3
Specific surface area (SSA), total and micropore volume (V_{pore}) and average pore width (d_{pores}) of different catalysts.

Catalyst	SSA[a]	V_{pores}[b] [cm^3/g]		d_{pores}[c]
	[m^2/g]	V_{tot}	V_{micro}	[nm]
$TS1_1$	514	0.305	0.245	0.62
$0.5Au_{90}Pd_{10}$-$TS1_1$-N	441	0.288	0.219	0.62
$0.5Au_{90}Pd_{10}$-$TS1_1$-W	439	0.286	0.221	0.62
$0.5Au_{90}Pd_{10}$-$TS1_1$-4	405	0.269	0.200	0.62
$0.5Au_{90}Pd_{10}$-$TS1_1$-18	415	0.280	0.208	0.61
$0.5Au_{95}Pd_{05}$-$TS1_1$	415	0.279	0.208	0.62
$TS1_2$	441	0.256	0.22	0.62
$0.5Au_{95}Pd_{05}$-$TS1_2$	412	0.254	0.206	0.61
$1.0Au_{90}Pd_{10}$-$TS1_2$	426	0.259	0.213	0.61
$1.0Au_{95}Pd_{05}$-$TS1_2$	430	0.258	0.214	0.61
$1.0Au_{100}$-$TS1_2$	434	0.263	0.218	0.61
$0.5Au_{90}Pd_{10}$-$TS1_2$-W	435	0.262	0.219	0.62
$0.5Au_{90}Pd_{10}$-$TS1_2$-nw	437	0.265	0.218	0.61

[a] Calculated with Dubinin-Radushkevich method.
[b] Calculated with Tarazona NLDFT method.
[c] Calculated with Horvath-Kawavoe method.

features, which could not be identified in this study, significantly improved the catalyst stability.

3.2.2. Impact of support, alloy composition, and metal loading

The influence of anatase-containing ($TS1_1$) versus anatase-free ($TS1_2$) TS-1 was studied by comparing $0.5Au_{90}Pd_{10}$-$TS1_1$-18 with $0.5Au_{90}Pd_{10}$-$TS1_2$-W, which have the same nominal metal loading and metal composition, and $0.5Au_{95}Pd_{05}$-$TS1_1$ with $0.5Au_{95}Pd_{05}$-$TS1_2$.

In both comparisons, the H_2 conversion was higher for the catalyst prepared with anatase-free TS-1 (Au_xPd_y-$TS1_2$) (Fig. 13), due to smaller AuPd nanoparticle (Table 2), providing a larger active surface for hydrogen activation. This correlates with higher propane (PA) and water productivities (Fig. 14) originating from the H_2 oxidation or H_2O_2 hydrogenation.The detection of H_2O_2 over the entire experiment with $0.5Au_{90}Pd_{10}$-$TS1_1$-18 and $0.5Au_{95}Pd_{05}$-$TS1_1$ (S 5) compared to the absences of unreacted H_2O_2 with $0.5Au_{90}Pd_{10}$-$TS1_2$-W and $0.5Au_{95}Pd_{05}$-$TS1_2$, confirm the higher H_2O_2 hydrogen activity with smaller AuPd nanoparticles. The higher metal loading (0.06 wt%) of $0.5Au_{95}Pd_{05}$-$TS1_2$ increased further the H_2 conversion compared to $0.5Au_{95}Pd_{05}$-$TS1_1$. The final PO productivity is higher with $0.5Au_{90}Pd_{10}$-$TS1_1$-18, however, when the ring opening products (ROP) are accounted for as secondary product of PO, $0.5Au_{90}Pd_{10}$-$TS1_2$-W exhibited a higher primary PO productivity, defined as the sum of PO and ROP, as illustrated in Fig. 14. 1-Methoxy-2-propanol and 2-methoxy-1-propanol, which are the observed ROP, are formed when the PO residence time is sufficiently long for the Lewis-acid sites of TS-1 to activate the epoxide ring towards a nucleophile addition. This can occur with methanol to form methoxypropanol or water to form propylene glycol. The latter is not occurring under these conditions as water is present in much lower concentration than methanol and has weaker nucleophile features. The increased ROP formation is likely due to an earlier H_2O_2 formation and consequently PO formation in the catalyst bed, which increases the residence time of PO and promotes its ring opening. Another factor might be the more compact structure of $TS1_2$ crystals compared to the open and mesoporous structure of $TS1_1$, as seen in Fig. 8a, which leads to longer residence times of PO within micropores, promoting the formation of ROP [46].

The activation observed for $0.5Au_{90}Pd_{10}$-$TS1_2$-W, compared to the stable PO production of $0.5Au_{90}Pd_{10}$-$TS1_1$-18, is likely due to the growth of small AuPd nanoparticles, which can be more selective towards the H_2O_2 formation and discussed further in Section 3.2.6. In contrast, the AuPd nanoparticle in $0.5Au_{90}Pd_{10}$-$TS1_1$-18 were already about three times larger before the reaction and therefore more selective, leading to a stable PO production. When comparing $0.5Au_{95}Pd_{05}$-$TS1_1$ with $0.5Au_{95}Pd_{05}$-$TS1_2$, a similar trend was observed; the anatase-free catalyst $0.5Au_{95}Pd_{05}$-$TS1_2$ exhibited higher PA and primary PO productivity along with no detectable H_2O_2 formation, being consistent with the comparison of $0.5Au_{90}Pd_{10}$-$TS1_1$-18 and $0.5Au_{90}Pd_{10}$-$TS1_2$-W. The different deactivation rates of $0.5Au_{95}Pd_{05}$-$TS1_1$ and $0.5Au_{95}Pd_{05}$-$TS1_2$, Fig. 15, are discussed in Section 3.2.6.

The influence of different alloys on the system was investigated using $1.0Au_{90}Pd_{10}$-$TS1_2$, $1.0Au_{95}Pd_{05}$-$TS1_2$ and $1.0Au_{100}$-$TS1_2$, with measured 0.60 wt% $Au_{85}Pd_{15}$, 0.89 wt% $Au_{95}Pd_{05}$ and 1.0 wt% Au_{100}, respectively. Catalysts prepared with the same TS-1 lot, $0.5Au_{90}Pd_{10}$-$TS1_1$-18 (0.39 wt% $Au_{89}Pd_{11}$) versus $0.5Au_{95}Pd_{05}$-$TS1_1$ (0.35 wt% $Au_{95}Pd_{05}$), and $0.5Au_{90}Pd_{10}$-$TS1_2$-W (0.35 wt% $Au_{90}Pd_{10}$) versus $0.5Au_{95}Pd_{05}$-$TS1_2$ (0.41 wt% $Au_{95}Pd_{05}$) are compared in addition. The monometallic gold catalyst $1.0Au_{100}$-$TS1_2$, designed to suppress the Pd-catalyzed propene hydrogenation and water formation, exhibited a low initial activity, and became completely inactive after 180 min TOS (Fig. 15), highlighting the necessity of Pd for hydrogen activation. In the comparison of the bimetallic catalysts, a lower Pd fraction in the alloy

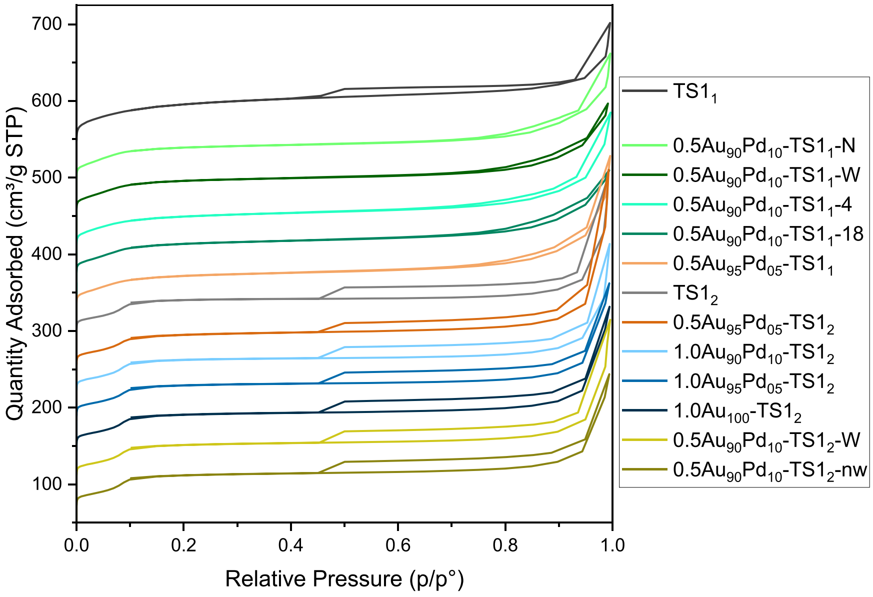

Fig. 11. Physisorption isotherms of investigated catalysts and TS-1 materials.

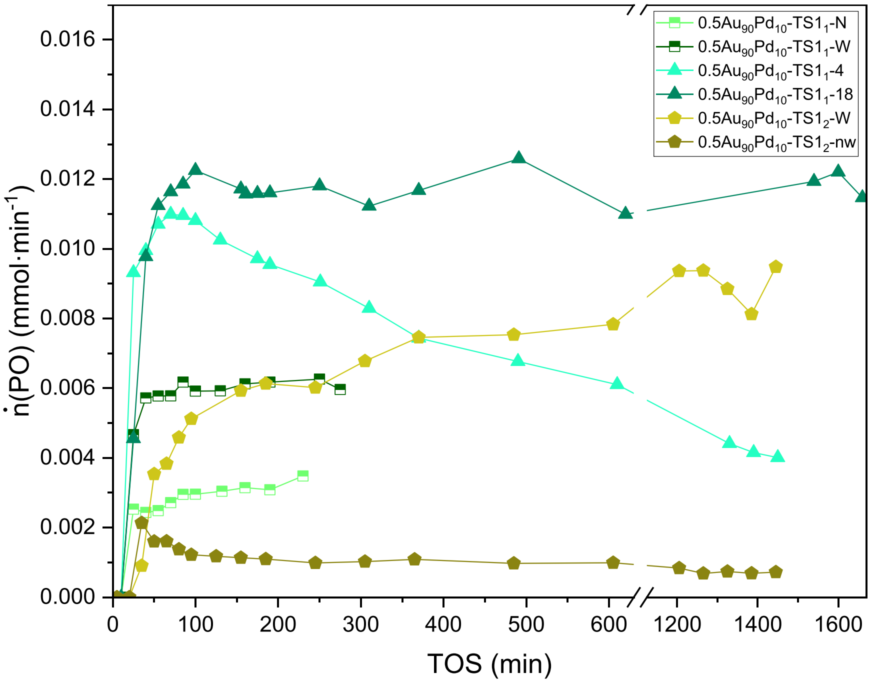

Fig. 12. PO production over time-on-stream (TOS) in HyPO using 1 g of different catalysts. In HyPO with $0.5Au_{90}Pd_{10}$-$TS1_1$-N and -W (half-filled squares), 0.5 g catalyst was used. Gas feed: H_2 (0.07 mmol·min^{-1}), O_2 (0.07 mmol·min^{-1}), propene (0.11 mmol·min^{-1} for $0.5Au_{90}Pd_{10}$-$TS1_1$-N, -W, −4 and −18; and 0.14 mmol·min^{-1} for $0.5Au_{90}Pd_{10}$-$TS1_2$-W and -nw) and CO_2 (1.46 mmol·min^{-1}). MeOH feed: 1 ml·min^{-1}. Reaction conditions: 10 °C, 8 bar.

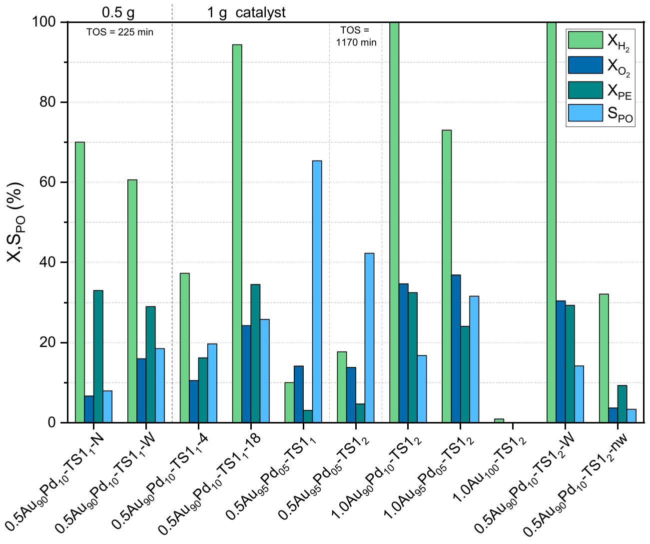

Fig. 13. Conversion of H_2 (light green), O_2 (blue) and propene (PE) (dark turquoise) and PO selectivity (light blue) with 0.5 g or 1 g catalyst and at TOS = 1420 min (except for three catalysts). Gas feed: H_2 (0.07 mmol·min^{-1}), O_2 (0.07 mmol·min^{-1}), propene (0.11 mmol·min^{-1} for $0.5Au_{90}Pd_{10}$-$TS1_1$-N, -W, −4, −18, $0.5Au_{95}Pd_{05}$-$TS1_1$ and -$TS1_2$; and 0.14 mmol·min^{-1} for $1.0Au_{90}Pd_{10}$-$TS1_2$, $1.0Au_{95}Pd_{05}$-$TS1_2$, $1.0Au_{100}$-$TS1_2$, $0.5Au_{90}Pd_{10}$-$TS1_2$-W and -nw) and CO_2 (1.46 mmol·min^{-1}). MeOH feed: 1 ml·min^{-1}. Reaction conditions: 10 °C, 8 bar.

reduced both the primary and final PO productivity (Fig. 14), due to a lower activity in H_2O_2 generation [14], reflected by the O_2 conversion (Fig. 13). The exceptions were $1.0Au_{90}Pd_{10}$-$TS1_2$ and $1.0Au_{95}Pd_{05}$-$TS1_2$, exhibiting similar O_2 conversions. Despite the lower loading of $1.0Au_{90}Pd_{10}$-$TS1_2$ compared to $1.0Au_{95}Pd_{05}$-$TS1_2$, the water formation is higher with similar O_2 consumption, which indicates an increased H_2O_2 hydrogenation with a Pd-richer alloy, reflected in the absence of unreacted H_2O_2 after the spike in the beginning, whereas with $1.0Au_{95}Pd_{05}$-$TS1_2$ is detected during the entire reaction (S 5). The synergetic effect of gold in alloys for DSHP is well known, as gold suppresses the O-O cleavage, responsible for water formation [14]. At the same time of the decreased PO productivity, the PO selectivity increased markedly with a decreasing Pd content, as water and PA formation were strongly suppressed, resulting in the highest selectivity (> 30 % S_{PO}) achieved among the synthesized catalysts, as illustrated in Fig. 13.

The influence of the catalysts metal loading on HyPO can be assessed by comparing $0.5Au_{95}Pd_{05}$-$TS1_2$ with $1.0Au_{95}Pd_{05}$-$TS1_2$, and $0.5Au_{90}Pd_{10}$-$TS1_2$-W with $1.0Au_{90}Pd_{10}$-$TS1_2$. For catalysts with less active $Au_{95}Pd_{05}$ alloy, the higher metal loading enhanced the productivity of all products (Fig. 14). The result suggests that $0.5Au_{95}Pd_{05}$-$TS1_2$ suffers from a limited H_2O_2 formation due to a lack of available active sites for DSHP, consistent with the nearly threefold higher O_2 conversion for $1.0Au_{95}Pd_{05}$-$TS1_2$ at double the metal loading, despite its larger AuPd nanoparticles. However, the PO selectivity decreased for $1.0Au_{95}Pd_{05}$-$TS1_2$ compared to $0.5Au_{95}Pd_{05}$-$TS1_2$, due to higher PA and ROP productivities, as the smaller AuPd nanoparticles of $0.5Au_{95}Pd_{05}$-$TS1_2$ exhibit higher hydrogenation activity and promote faster PO formation. In contrast, for the catalysts with the more active alloys $Au_{85}Pd_{15}$ ($1.0Au_{90}Pd_{10}$-$TS1_2$) and $Au_{90}Pd_{10}$ ($0.5Au_{90}Pd_{10}$-$TS1_2$-W), a higher metal loading reduced the productivity of all the products, as the lower loaded $0.5Au_{90}Pd_{10}$-$TS1_2$-W already achieved a complete H_2 conversion with less available active sites.

In conclusion, the investigation of the support material, alloy, and metal loading, demonstrated that the support has a significant influence on the metal nanoparticle size, which governs the reaction system. Smaller AuPd nanoparticles exhibited an increased activity towards hydrogenation due to a more accessible active surface for DHSP. However, for the H_2O_2 synthesis, moderate activity is crucial, which suppresses overoxidation to water, a behavior observed for catalysts with larger nanoparticles. The alloy further controlled the activity of the metal nanoparticles, where a lower Pd content of the alloy decreased the possibility of hydrogenation and therefore clearly increased the selectivity of H_2O_2 and PO by suppressing water and propane formation.

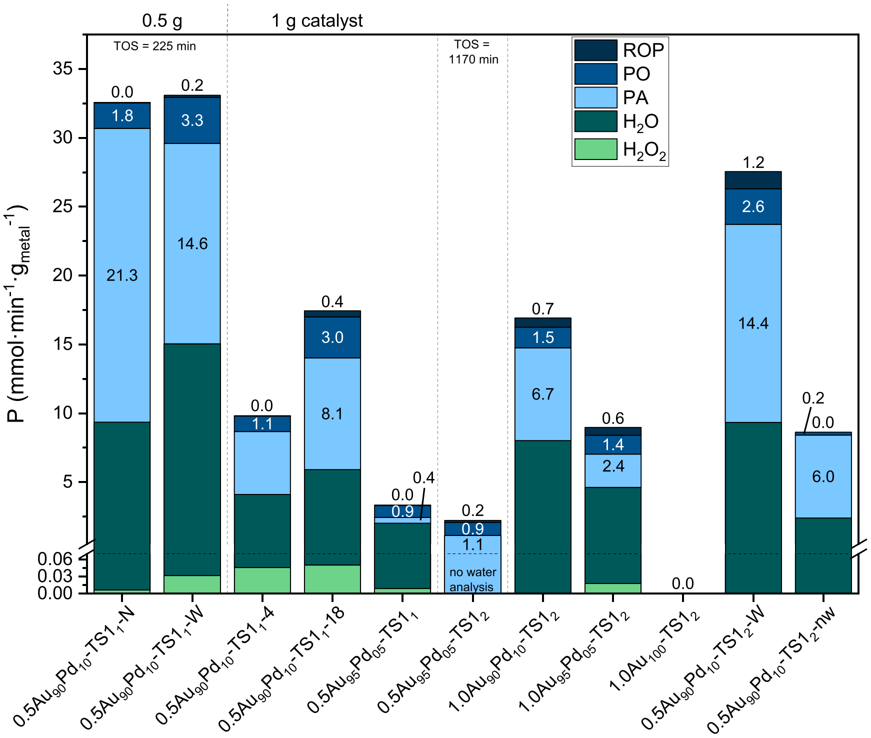

Fig. 14. Productivity of H_2O_2 (light green), H_2O (dark turquoise), ROP (dark blue), PO (blue), and PA (light blue) in HyPO using 0.5 g or 1.0 g catalyst and at TOS = 1420 min (except for three catalysts)·H_2O_2 productivity of 0.5Au$_{90}$Pd$_{10}$-TS1$_1$-18 was taken at TOS = 600 min. Gas feed: H_2 (0.07 mmol·min^{-1}), O_2 (0.07 mmol·min^{-1}), propene (0.11 mmol·min^{-1} for 0.5Au$_{90}$Pd$_{10}$-TS1$_1$-N, -W, −4, −18, 0.5Au$_{95}$Pd$_{05}$-TS1$_1$ and -TS1$_2$; and 0.14 mmol·min^{-1} for 1.0Au$_{90}$Pd$_{10}$-TS1$_2$, 1.0Au$_{95}$Pd$_{05}$-TS1$_2$, 1.0Au$_{100}$-TS1$_2$, 0.5Au$_{90}$Pd$_{10}$-TS1$_2$-W and -nw) and CO_2 (1.46 mmol·min^{-1}). MeOH feed: 1 ml·min^{-1}. Reaction conditions: 10 °C, 8 bar.

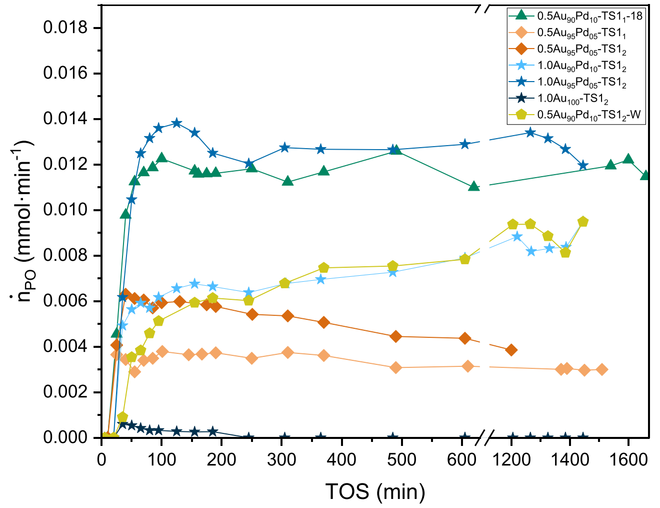

Fig. 15. PO production in HyPO using 1 g of different catalysts. Gas feed: H_2 (0.07 mmol·min^{-1}), O_2 (0.07 mmol·min^{-1}), propene (0.11 mmol·min^{-1} for 0.5Au$_{90}$Pd$_{10}$-TS1$_1$-18, 0.5Au$_{95}$Pd$_{05}$-TS1$_1$ and -TS1$_2$; and 0.14 mmol·min^{-1} for 1.0Au$_{90}$Pd$_{10}$-TS1$_2$, 1.0Au$_{95}$Pd$_{05}$-TS1$_2$, 1.0Au$_{100}$-TS1$_2$ and 0.5Au$_{90}$Pd$_{10}$-TS1$_2$-W) and CO_2 (1.46 mmol·min^{-1}). MeOH feed: 1 ml·min^{-1}. Reaction conditions: 10 °C, 8 bar.

Increasing the metal loading was only beneficial when the activity of the metal particles, directed by size and alloy, was moderate.

3.2.3. Impact of temperature

The influence of temperature on HyPO was investigated between 0 and 20 °C. The PO production increased steadily from 0 to 10 °C, but increased only slowly toward 20 °C, consistent with the onset and increase of the ROP formation at 10 °C (Fig. 16). With an increasing temperature, more rapid reactions shifted the product distribution along the reaction sequence $H_2+O_2 \longrightarrow H_2O_2 \longrightarrow PO \longrightarrow ROP$, underlining the consecutive reaction system of HyPO. The PA production reaches a maximum at 10 °C, probably because the H_2 oxidation and/or H_2O_2 hydrogenation became more dominating at higher temperatures, consistent with the increasing water formation. In parallel, the combined effects of increasing H_2O_2 consumption in the epoxidation and H_2O_2 hydrogenation accounted for the steady decline of detectable H_2O_2 with increasing temperature.

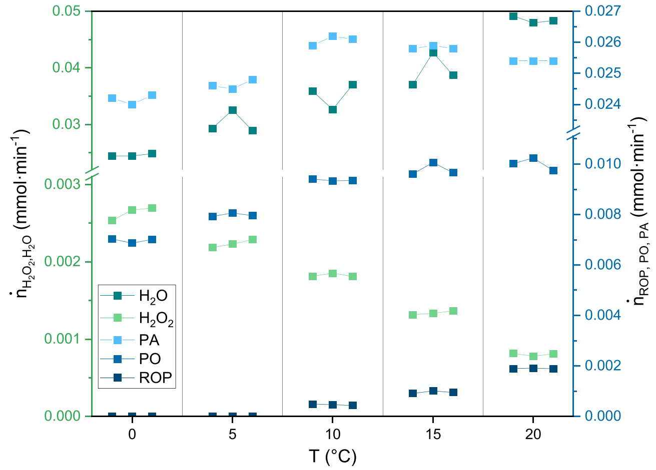

Fig. 16. Production of H_2O_2 (green), H_2O (dark turquoise), ROP (dark blue), PO (blue), and PA (light blue) using 0.78 g 0.5Au$_{90}$Pd$_{10}$-TS1$_1$-18 in HyPO at different temperatures. Gas feed: H_2 (0.07 mmol·min^{-1}), O_2 (0.07 mmol·min^{-1}), propene (0.11 mmol·min^{-1}) and CO_2 (1.46 mmol·min^{-1}). MeOH feed: 1 ml·min^{-1}. Pressure: 8 bar.

3.2.4. *Impact of liquid flow rate*

The influence of the liquid flow rate was studied to assess the effect of residence time on the product distribution (Fig. 17). Lowering the MeOH flow rate decreased the unreacted H_2O_2 and increased the ROP formation, similar to the trend observed with an increasing temperature. In contrast, the PO production reached a maximum at 1 ml·min^{-1}, but declined at lower flow rates as PO reacted further to ROP due to a longer residence time. The primary PO production, the sum of PO and ROP, decreased at a flow rate of 0.5 ml·min^{-1} compared to 1.0 ml·min^{-1}, suggesting a lower H_2O_2 utilization for epoxidation, as a longer residence time promotes the AuPd-catalyzed degradation of H_2O_2 to water. Contrary, more hydrogenation products, water and propane, are observed with higher liquid flow, which can be explained by a reduced mass transfer resistancefrom gas to liquid phase, which is also reflected in the increased hydrogen conversion (60 % with 0.5 ml·min^{-1}, 86 % with 1.0 ml·min^{-1} and 96 % with 2.0 ml·min^{-1}). The highest PA formation was observed at the highest MeOH flow rate, which aligns with the reduced mass transfer residence.

3.2.5. *Impact of reactant feed composition*

The reactant feed composition was varied to promote DSHP and suppress propene hydrogenation. Switching from a propene-rich to the 1:1:0.8 H_2/O_2/propene composition reduced the PA production but lowered the PO production, while the H_2O_2 production increased twofold (Fig. 18). An oxygen-rich composition reduced the PA formation and surprisingly H_2O_2 formation compared to the 1:1:0.8 feed composition, likely due to competitive oxygen coverage suppressing the hydrogenation activation [47]. When shifting from a propene-rich to an oxygen-rich feed composition the PO selectivity increased only slightly from 24.6 % to 28.6 %, however, the suppression of propene hydrogenation and the increased amount of unreacted H_2O_2 suggest a potentially more efficient system if the remained H_2O_2 will be converted by tuning other reaction parameters, such as temperature or liquid flow rate.

3.2.6. *Catalyst deactivation*

The spent catalysts were characterized to elucidate the activation and deactivation processes in HyPO. ICP analysis revealed, that metal leaching occurred in all the catalysts and was most pronounced for the highest loaded catalysts 1.0Au$_{95}$Pd$_{05}$-TS1$_2$ (initially 0.89 wt%), and 1.0Au$_{100}$-TS1$_2$ (initially 1.0 wt%), which lost −45 % and −50 % of their metal content, respectively (Fig. 19). Catalysts with a nominal loading of 0.5 wt% and 1.0Au$_{95}$Pd$_{05}$-TS1$_2$ showed lower leaching, between 7 % and 33 %.

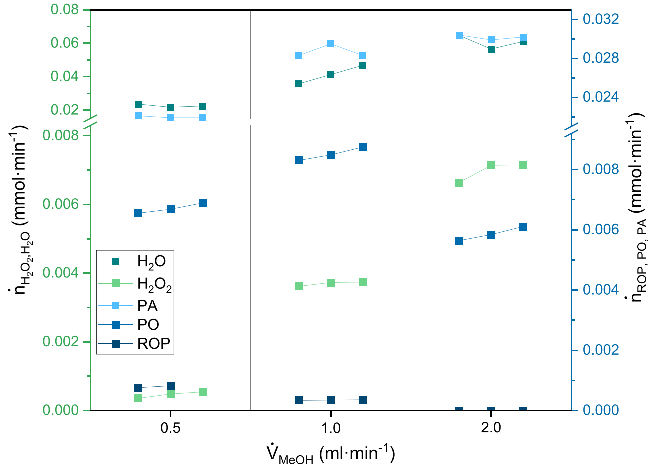

Fig. 17. Production of H_2O_2 (green), H_2O (dark turquoise), ROP (dark blue), PO (blue), and PA (light blue) using 0.78 g 0.5Au$_{90}$Pd$_{10}$-TS1$_1$-18 in HyPO at different MeOH flow rates. Gas feed: H_2 (0.07 mmol·min^{-1}), O_2 (0.07 mmol·min^{-1}), propene (0.11 mmol·min^{-1}), and CO_2 (1.46 mmol·min^{-1}). Reaction conditions: 10 °C, 8 bar.

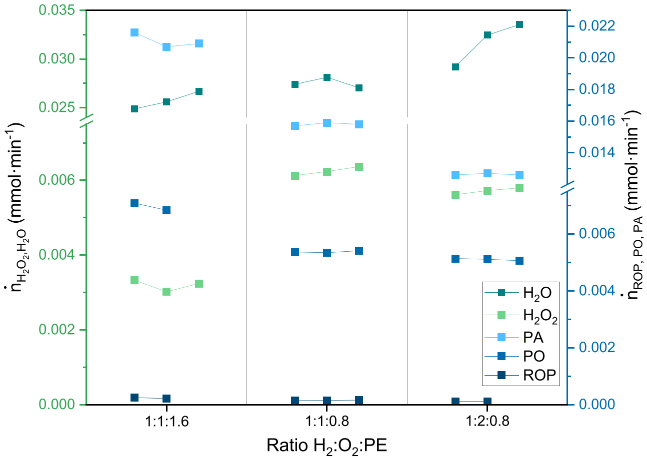

Fig. 18. Production of H_2O_2 (green), H_2O (dark turquoise), ROP (dark blue), PO (blue), and PA (light blue) using 0.78 g 0.5Au$_{90}$Pd$_{10}$-TS1$_1$-18 in HyPO. 1:1:1.6 gas feed: H_2 (0.07 mmol·min^{-1}), O_2 (0.07 mmol·min^{-1}), propene (0.11 mmol·min^{-1}) and CO_2 (1.46 mmol·min^{-1}); 1:1:0.8 gas feed: H_2 and O_2 (each 0.07 mmol·min^{-1}), propene (0.06 mmol·min^{-1}) and CO_2 (1.52 mmol·min^{-1}); and 1:2:0.8 gas feed: H_2 (0.07 mmol·min^{-1}), O_2 (0.14 mmol·min^{-1}), propene (0.06 mmol·min^{-1}) and CO_2 (1.46 mmol·min^{-1}). MeOH feed: 1 ml·min^{-1}. Reaction conditions: 10 °C, 8 bar.

The AuPd nanoparticle size analysis of the spent catalyst showed a much stronger size increase for nanoparticles deposited on anatase compared to those on TS-1. The higher nanoparticle density on anatase promotes sintering, particularly evident in the spent catalysts 0.5Au$_{90}$Pd$_{10}$-TS1$_1$-N and 0.5Au$_{90}$Pd$_{10}$-TS1$_1$-W, which were only used for less than 280 min in HyPO. In contrast, the decrease of AuPd nanoparticles on TS-1 was observed in several catalysts (0.5Au$_{90}$Pd$_{10}$-TS1$_1$-N, 0.5Au$_{90}$Pd$_{10}$-TS1$_1$-W, 1.0Au$_{95}$Pd$_{05}$-TS1$_2$ and 1.0Au$_{100}$-TS1$_2$), likely resulting from preferential leaching of larger nanoparticles. However, precise size determination of AuPd on anatase is challenging due to overlapping nanoparticles, as seen in S 6, and the reported Feret diameter does not fully capture the extent of particle coalescence or the associated loss of active surface.

In the DSHP process, the metal nanoparticles growth can exert two opposing effects; a reduced activity and an increased H_2O_2 selectivity, as larger nanoparticles are less active and suppress overoxidation to water. Although several studies have reported increased H_2O_2 productivity and selectivity with decreasing AuPd particle size [45], the observed activations in PO production for 1.0Au$_{90}$Pd$_{10}$-TS1$_2$ and 0.5Au$_{90}$Pd$_{10}$-TS1$_2$-W, directly correlated to H_2O_2 productivity, likely originated from the opposite effect. In our system, the growth of the more active Pd-rich nanoparticles likely enhanced H_2O_2 selectivity sufficiently to outweigh the loss of activity. These two catalysts also possessed the smallest AuPd nanoparticles among the catalysts, supporting our interpretation. The size effect on catalyst performance is further influenced by factors such as alloy composition, support material, and reactor system (batch or continuous), challenging the confirmation of our interpretation, as systems closely resembling ours have not been reported in the literature. In contrast to the Pd-rich catalysts, the catalysts 0.5Au$_{95}$Pd$_{05}$-TS1$_1$ and 0.5Au$_{95}$Pd$_{05}$-TS1$_2$, with less active Au-richer alloy, showed deactivation, as their selectivity was already enhanced due to a reduced hydrogen activation. The different deactivation rates between those two catalysts likely originate from the much smaller AuPd nanoparticles of 0.5Au$_{95}$Pd$_{05}$-TS1$_2$, which suffered a higher activity loss upon growth, even though the nanoparticle size increase was higher in 0.5Au$_{95}$Pd$_{05}$-TS1$_1$. Deactivation among catalysts with Pd-richer alloy was observed only for 0.5Au$_{90}$Pd$_{10}$-TS1$_1$-4 and 0.5Au$_{90}$Pd$_{10}$-TS1$_2$-nw, both of which were synthesized with

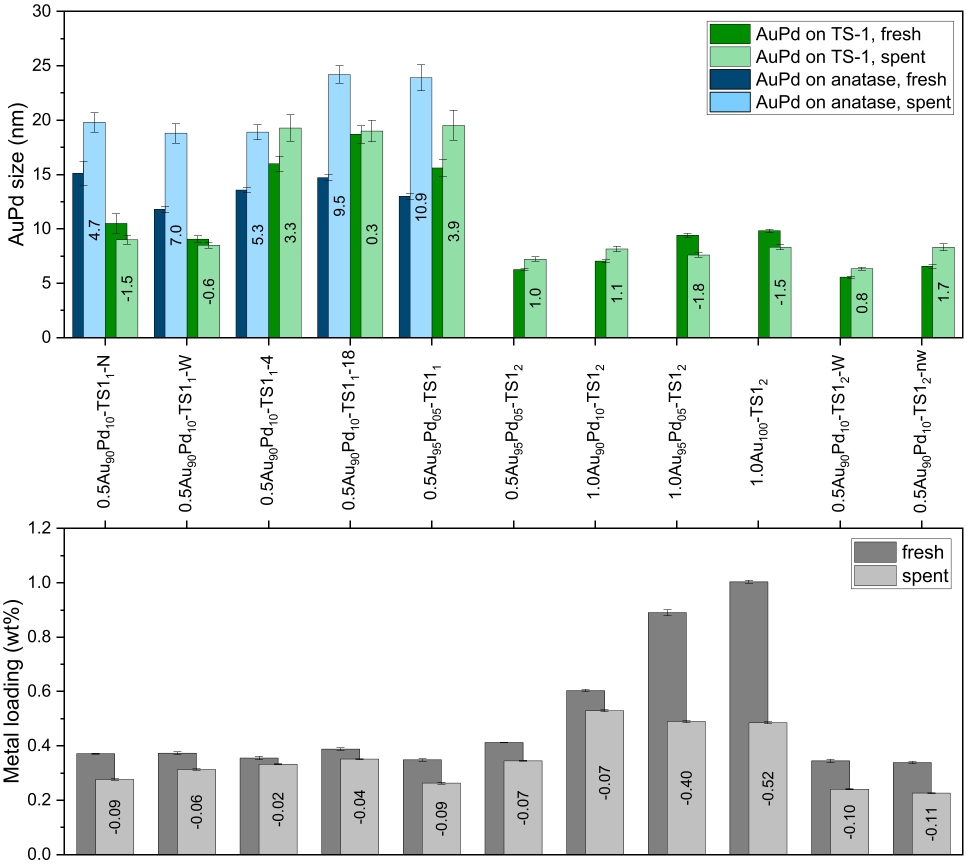

Fig. 19. The AuPd nanoparticle mean sizes of different catalysts before (darker color) and after usage (lighter color) in HyPO is illustrated in the upper graph. The size changes, labeled in the bars, of AuPd nanoparticles on TS-1 (green) and on anatase (blue) are shown. The metal loading changes, labeled in the bars, of different catalysts before (dark grey) and after (light grey) reaction are shown in the lower graph.

non-standard procedure (shorter synthesis time and omission of washing). For 0.5$Au_{90}Pd_{10}$-TS1_1-18, the two opposing effects of nanoparticle growth might compensate each other, resulting in stable PO production.

The cause of the gradual deactivation of 0.5$Au_{90}Pd_{10}$-TS1_1-4 compared to −18, remained unclear, as both catalysts exhibited similar metal leaching and growth of AuPd nanoparticles on anatase. Additional characterization of the spent catalysts by XPS, temperature programmed desorption (TPD) and ICP analysis of the catalyst bed sand did not provide further information about catalyst deactivation or activation in HyPO.

The specific surface area (SSA) was measured of selected spent catalysts and found to be reduced, likely due to pore blockage by ROP or higher condensation products [48]. The highest losses (104 $m^2 \cdot g^{-1}$) were observed for 1.0$Au_{95}Pd_{05}$-TS1_2 and 0.5$Au_{90}Pd_{10}$-TS1_2-W, which also showed the highest ROP production (5.0 and 4.5 μmol·min^{1-}, respectively). In contrast, 0.5$Au_{90}Pd_{10}$-TS1_1-18 lost only 44 $m^2 \cdot g^{-1}$ and formed just 1.7 μmol·min^{1-} ROP. Interestingly, 0.5$Au_{95}Pd_{05}$-TS1_1 and 0.5$Au_{95}Pd_{05}$-TS1_2 showed relatively low ROP productions (0.1 and 0.6 μmol·min^{-1}, respectively) despite higher SSA losses (60 and 68 $m^2 \cdot g^{-1}$).

4. Conclusion

Several AuPd/TS-1 catalysts were synthesized and optimized for the one-pot direct synthesis of hydrogen peroxide and epoxidation of propene in liquid phase under mild conditions (HyPO). The catalyst performance strongly depended on the synthesis parameters, with water-only washing and longer synthesis times yielding the most active and stable catalysts. The anatase impurities in TS-1 promoted non-uniform metal deposition, while anatase-free supports enabled smaller, more dispersed AuPd nanoparticles. The catalytic activity and selectivity depended on a complex interplay of nanoparticle size, alloy composition, and metal loading, with larger nanoparticle and gold-richer alloys favoring the PO selectivity, while smaller nanoparticles with higher Pd content enhanced the PO production. Optimization of reaction temperature, liquid flow and reactant composition provided insights into the process dynamics of HyPO and identified 10 °C and 1 ml/min methanol flow as optimal conditions, and shifting from propene-rich to oxygen-rich feed improved slightly the PO selectivity. This study identified the key parameters influencing HyPO and deepened the understanding of the process dynamics. Further process intensification may be achieved with systematic studies of alloy and nanoparticle size dependency, as well as catalyst bed engineering using mixed catalysts and modified packing structures.

CRediT authorship contribution statement

Tapio Salmi: Writing – original draft, Validation, Supervision, Resources, Project administration, Methodology, Investigation, Funding acquisition, Formal analysis, Conceptualization. **Mika Lastusaari:** Visualization, Validation, Methodology, Investigation, Formal analysis, Data curation, Conceptualization. **Sari Granroth:** Visualization, Validation, Methodology, Investigation, Formal analysis, Data curation, Conceptualization. **Francesco Sandri:** Writing – original draft, Visualization, Validation, Software, Methodology, Investigation, Formal analysis, Data curation, Conceptualization. **Christoph Schmidt:** Writing – original draft, Visualization, Validation, Supervision, Software, Methodology, Investigation, Formal analysis, Data curation, Conceptualization. **Atte Aho:** Visualization, Validation, Methodology, Investigation, Formal analysis, Data curation. **Jeremy Favier:**

Visualization, Validation, Methodology, Investigation, Formal analysis, Data curation. **Alice Vidrequin:** Visualization, Validation, Methodology, Investigation, Formal analysis, Data curation.

Declaration of Competing Interest

The authors declare that they have no known competing financial interests or personal relationships that could have appeared to influence the work reported in this paper.

Acknowledgement

Part of the research has been financed by Academy of Finland, through the Academy Professor grants 319002, 320115 and 361253 (T. S. and C.S.). Materials research infrastructure/Department of Physics and Astronomy, University of Turku is gratefully acknowledged for the possibility to use their XPS.

Appendix A. Supporting information

Supplementary data associated with this article can be found in the online version at doi:10.1016/j.apcata.2025.120756.

Data availability

Data will be made available on request.

References

[1] V. Russo, R. Tesser, E. Santacesaria, M. Di Serio, Chemical and technical aspects of propene oxide production via hydrogen peroxide (HPPO Process), Ind. Eng. Chem. Res 52 (2013) 1168–1178, https://doi.org/10.1021/ie3023862.

[2] T. Miyazaki, S. Ozturk, I. Onal, S. Senkan, Selective oxidation of propylene to propylene oxide using combinatorial methodologies, Catal. Today 81 (2003) 473–484, https://doi.org/10.1016/S0920-5861(03)00146-9.

[3] D.L. Trent, Propylene Oxide, Kirk. -Othmer Encycl. Chem. Technol. (2001), https://doi.org/10.1002/0471238961.1618151620180514.a01.pub2.

[4] SrL I.P.T. The Growing Impact of Propylene Oxide Applications 2024. 〈https://www.iptsrl.com/2024/12/12/the-growing-impact-of-propylene-oxide-applications/〉 (accessed May 22, 2025).

[5] T.A. Nijhuis, M. Makkee, J.A. Moulijn, B.M. Weckhuysen, The production of propene oxide: catalytic processes and recent developments, Ind. Eng. Chem. Res 45 (2006) 3447–3459, https://doi.org/10.1021/ie0513090.

[6] P. Bassler, M. Weidenbach, H. Goebbel, He new hppo process for propylene oxide: from joint development to worldscale production, Chem. Eng. Trans. 21 (2010) 571–576, https://doi.org/10.3303/CET1021096.

[7] Thyssenkrupp. Propylene oxide - The clean Evonik-Uhde HPPO technology n.d. 〈https://www.thyssenkrupp-uhde.com/en/products-and-technologies/polymers-and-plastics-technologies/propylene-oxide-hppo〉 (accessed June 9, 2025).

[8] M. Alvear, C. Schmidt, O. Reinsdorf, E. Lebron-Rodrigez, A. Al Abdulghani, I. Hermans, et al., Ti-MWW Catalysts for Propylene Oxide Production: influence of Si/Ti Ratio and Calcination Conditions, Catal. Lett. 154 (2024) 834–845, https://doi.org/10.1007/s10562-023-04350-x.

[9] D. Lin, X. Feng, Y. Xu, R.J. Lewis, X. Chen, T.E. Davies, et al., Radical-constructed intergrown titanosilicalite interfaces for efficient direct propene epoxidation with H2 and O2, Nat. Commun. 16 (2025) 5515, https://doi.org/10.1038/s41467-025-60637-0.

[10] K.H. Kim, S.W. Hwang, T. Kim, H. Kim, M. Ko, S.S. Yoon, et al., Self-driven propylene epoxidation on modified titanium silicalite-1 by in situ generated hydrogen peroxide, Nat. Commun. 16 (2025) 8636, https://doi.org/10.1038/s41467-025-63828-x.

[11] C. Stäglich, M. Alvear, C. Schmidt, I. Angervo, V. Russo, S. Haase, et al., Trickle bed reactor technology for propylene epoxidation with extrudates – Catalyst characterization, kinetic studies and modelling, Chem. Eng. Sci. 310 (2025) 121570, https://doi.org/10.1016/j.ces.2025.121570.

[12] M. Alvear, J. Lopez-Gonzalez, C. Stäglich, A.J. Al Abdulghani, K. Eränen, S. Haase, et al., Ammonia: a vital additive in the epoxidation of propylene over TS-1 extrudates, Chem. Eng. J. 506 (2025) 160229, https://doi.org/10.1016/j.cej.2025.160229.

[13] DOW, Basf to build propylene oxide, Chem. Eng. N. Arch. 82 (2004) 15, https://doi.org/10.1021/cen-v082n036.p015a.

[14] T. Richards, R.J. Lewis, D.J. Morgan, G.J. Hutchings, The direct synthesis of hydrogen peroxide over supported pd-based catalysts: an investigation into the role of the support and secondary metal modifiers, Catal. Lett. 153 (2023) 32–40, https://doi.org/10.1007/s10562-022-03967-8.

[15] T. Hayashi, K. Tanaka, M. Haruta, HydrogenSelective vapor-phase epoxidation of propylene over Au/TiO2Catalysts in the presence of oxygen, J. Catal. 178 (1998) 566–575, https://doi.org/10.1006/jcat.1998.2157.

[16] W. Li, L. Chen, M. Qiu, W. Li, Y. Zhang, Y. Zhu, et al., Highly efficient epoxidation of propylene with in situ-generated H2O2 over a hierarchical TS-1 zeolite-supported non-noble nickel catalyst, ACS Catal. 13 (2023) 10487–10499, https://doi.org/10.1021/acscatal.3c02206.

[17] C. Zhao, Y. Liu, Y. Tian, Y. Li, J. Feng, W. Xu, et al., Enhanced catalytic performance for gas phase epoxidation of propylene with H2 and O2 by multiple pretreated Au/TS-1 catalysts, Appl. Catal. A Gen. 685 (2024) 119895, https://doi.org/10.1016/j.apcata.2024.119895.

[18] G. Jenzer, T. Mallat, M. Maciejewski, F. Eigenmann, A. Baiker, Continuous epoxidation of propylene with oxygen and hydrogen on a Pd–Pt/TS-1 catalyst, Appl. Catal. A Gen. 208 (2001) 125–133, https://doi.org/10.1016/S0926-860X(00)00689-X.

[19] A. Prieto, M. Palomino, U. Díaz, A. Corma, One-pot two-step process for direct propylene oxide production catalyzed by bi-functional Pd(Au)@TS-1 materials, Appl. Catal. A Gen. 523 (2016) 73–84, https://doi.org/10.1016/j.apcata.2016.05.019.

[20] Schmidt C., Alvear M., Sandri F., Mandon S., Ojala S., Laitinen T., et al. New bi-functional catalysts for a novel continuous production of propylene oxide with in-situ generated hydrogen peroxide. J Catal n.d. https://doi.org/10.1016/j.jcat.2025.116637.

[21] T. Degen, M. Sadki, E. Bron, U. König, G. Nénert, The HighScore suite, Powder Diffr. 29 (2014) S13–S18, https://doi.org/10.1017/S0885715614000840.

[22] S. Gates-Rector, T. Blanton, The Powder Diffraction File: a quality materials characterization database, Powder Diffr. 34 (2019) 352–360, https://doi.org/10.1017/S0885715619000812.

[23] R.H. Perry, D.W. Green, Seventh Ed. Perry's Chemical Engineers' Handbook, McGraw-Hill International Edition, 1997.

[24] F. Sandri, M. Danieli, M. Zecca, P. Centomo, Comparing catalysts of the direct synthesis of hydrogen peroxide in organic solvent: is the measure of the product an issue? ChemCatChem 13 (2021) 2653–2663, https://doi.org/10.1002/cctc.202100306.

[25] Z.K. Lopez-Castillo, S.N.V.K. Aki, M.A. Stadtherr, J.F. Brennecke, Enhanced solubility of hydrogen in CO2-expanded liquids, Ind. Eng. Chem. Res. 47 (2008) 570–576, https://doi.org/10.1021/ie070105b.

[26] J. De Laat, G. Truong Le, B. Legube, A comparative study of the effects of chloride, sulfate and nitrate ions on the rates of decomposition of H2O2 and organic compounds by Fe(II)/H2O2 and Fe(III)/H2O2, Chemosphere 55 (2004) 715–723, https://doi.org/10.1016/j.chemosphere.2003.11.021.

[27] P. Biasi, J. García-Serna, A. Bittante, T. Salmi, Direct synthesis of hydrogen peroxide in water in a continuous trickle bed reactor optimized to maximize productivity, Green. Chem. 15 (2013) 2502–2513, https://doi.org/10.1039/C3GC40811F.

[28] M. Alvear, K. Eränen, D.Y. Murzin, T. Salmi, Study of the product distribution in the epoxidation of propylene over TS-1 catalyst in a trickle-bed reactor, Ind. Eng. Chem. Res 60 (2021) 2430–2438, https://doi.org/10.1021/acs.iecr.0c06150.

[29] R. Zanella, L. Delannoy, C. Louis, Mechanism of deposition of gold precursors onto TiO2 during the preparation by cation adsorption and deposition–precipitation with NaOH and urea, Appl. Catal. A Gen. 291 (2005) 62–72, https://doi.org/10.1016/j.apcata.2005.02.045.

[30] A. Wróblewska, J. Grzeszczak, P. Miądlicki, K. Kiełbasa, M. Kujbida, A. Kamińska, et al., The studies on α-pinene oxidation over the TS-1. The INfluence of the Temperature, Reaction Time, Titanium and Catalyst Content, Mater. 14 (2021), https://doi.org/10.3390/ma14247799.

[31] S. Ivanova, C. Petit, V. Pitchon, A new preparation method for the formation of gold nanoparticles on an oxide support, Appl. Catal. A Gen. 267 (2004) 191–201, https://doi.org/10.1016/j.apcata.2004.03.004.

[32] X. Lu, G. Zhao, Y. Lu, Propylene epoxidation with O2 and H2: a high-performance Au/TS-1 catalyst prepared via a deposition–precipitation method using urea, Catal. Sci. Technol. 3 (2013) 2906–2909, https://doi.org/10.1039/C3CY00339F.

[33] P. Verma, K. Mori, Y. Kuwahara, S.J. Cho, H. Yamashita, Synthesis of plasmonic gold nanoparticles supported on morphology-controlled TiO2 for aerobic alcohol oxidation, Catal. Today 352 (2020) 255–261, https://doi.org/10.1016/j.cattod.2019.10.014.

[34] S. Moussa, G. Atkinson, M. SamyEl-Shall, A. Shehata, K.M. AbouZeid, M. B. Mohamed, Laser assisted photocatalytic reduction of metal ions by graphene oxide, J. Mater. Chem. 21 (2011) 9608–9619, https://doi.org/10.1039/C1JM11228G.

[35] Z. Li, L. Gao, W. Ma, Q. Zhong, Higher gold atom efficiency over Au-Pd/TS-1 alloy catalysts for the direct propylene epoxidation with H2 and O2, Appl. Surf. Sci. 497 (2019) 143749, https://doi.org/10.1016/j.apsusc.2019.143749.

[36] A. Venäläinen, K. Meinander, M. Räisänen, V. Tuboltsev, J. Räisänen, Metallization of self-assembled organic monolayer surfaces by Pd nanocluster deposition, Surf. Sci. 677 (2018) 68–77, https://doi.org/10.1016/j.susc.2018.06.006.

[37] N. Kruse, S. Chenakin, XPS characterization of Au/TiO2 catalysts: Binding energy assessment and irradiation effects, Appl. Catal. A Gen. 391 (2011) 367–376, https://doi.org/10.1016/j.apcata.2010.05.039.

[38] Z. Gao, Y. Zhao, L. Yang, X. Peng, C. Xia, E. Xing, et al., Unraveling the Effect of Acid Treatment Prior to Alkaline Treatment on the Performance of TS-1 Zeolite, Catal. Lett. 154 (2024) 4729–4736, https://doi.org/10.1007/s10562-024-04680-4.

[39] Y. Yu, R. Wang, W. Liu, Z. Chen, H. Liu, X. Huang, et al., Control of Ti active-site microenvironment in titanosilicate catalysts and its effect on oxidation pathways, Appl. Catal. A Gen. 610 (2021) 117953, https://doi.org/10.1016/j.apcata.2020.117953.

[40] J. Sun, Z. Zhang, E. Yang, W. Du, F. Liu, K. Xu, et al., Trace Pd alloyed with Au to boost Au/uncalcined TS-1 catalyzed propane hydro-oxidation to acetone, Nano Res. 17 (2024) 7182–7193, https://doi.org/10.1007/s12274-024-6705-3.

[41] P. Marécot, A. Fakche, B. Kellali, G. Mabilon, P. Prigent, J. Barbier, Propane and propene oxidation over platinum and palladium on alumina: Effects of chloride and water, Appl. Catal. B Environ. 3 (1994) 283–294, https://doi.org/10.1016/0926-3373(94)00003-4.

[42] V.R. Choudhary, C. Samanta, Role of chloride or bromide anions and protons for promoting the selective oxidation of H2 by O2 to H2O2 over supported Pd catalysts in an aqueous medium, J. Catal. 238 (2006) 28–38, https://doi.org/10.1016/j.jcat.2005.11.024.

[43] L. Wu, X. Deng, S. Zhao, H. Yin, Z. Zhuo, X. Fang, et al., Synthesis of a highly active oxidation catalyst with improved distribution of titanium coordination states, Chem. Commun. 52 (2016) 8679–8682, https://doi.org/10.1039/C6CC03318K.

[44] J.K. Edwards, B.E. Solsona, P. Landon, A.F. Carley, A. Herzing, C.J. Kiely, et al., Direct synthesis of hydrogen peroxide from H2 and O2 using TiO2-supported Au–Pd catalysts, J. Catal. 236 (2005) 69–79, https://doi.org/10.1016/j.jcat.2005.09.015.

[45] J. Brehm, R.J. Lewis, D.J. Morgan, T.E. Davies, G.J. Hutchings, The direct synthesis of hydrogen peroxide over AuPd nanoparticles: an investigation into metal loading, Catal. Lett. 152 (2022) 254–262, https://doi.org/10.1007/s10562-021-03632-6.

[46] N. Sheng, D. Lin, W. Liang, C. Zhao, Y. Liu, Y. Zhu, et al., Intracrystalline diffusion regulation of Au/hierarchical TS-1 for simultaneously enhanced stability and selectivity in propene epoxidation with H2 and O2, Chem. Eng. Sci. 300 (2024) 120538, https://doi.org/10.1016/j.ces.2024.120538.

[47] A. Santos, R.J. Lewis, G. Malta, A.G.R. Howe, D.J. Morgan, E. Hampton, et al., Direct synthesis of hydrogen peroxide over Au–Pd supported nanoparticles under ambient conditions, Ind. Eng. Chem. Res 58 (2019) 12623–12631, https://doi.org/10.1021/acs.iecr.9b02211.

[48] Q. Wang, L. Wang, J. Chen, Y. Wu, Z. Mi, Deactivation and regeneration of titanium silicalite catalyst for epoxidation of propylene, J. Mol. Catal. A Chem. 273 (2007) 73–80, https://doi.org/10.1016/j.molcata.2007.03.068.